FINAL PUBLISHABLE REPORT

Grant Agreement number	20FUN05
Project short name	SEQUME
Project full title	Single- and entangled photon sources for quantum metrology

Project start date and duration:		01 June 2021, 36 months
Coordinator: Kück, Stefan, Dr., PTB Tel: ++49 531 592-4010 E-mail: Stefan.Kueck@ptb.de Project website address: https://sequme.cmi.cz/		
Internal Funded Partners: 1. PTB, Germany 2. Aalto, Finland 3. CMI, Czech Republic 4. DFM, Denmark 5. JV, Norway 6. Metrosert, Estonia 7. TUBITAK, Turkey	External Funded Partners: 8. CNR, Italy 9. CSIC, Spain 10. FAU, Germany 11. INFN, Italy 12. KBFI, Estonia 13. TUB, Germany 14. UdS, Germany 15. UNITO, Italy 16. USTUTT, Germany 17. ZIB, Germany	Unfunded Partners: 18. INRIM, Italy
RMGx: -		

TABLE OF CONTENTS

1 Overview

(Please leave this section blank. This section will be completed by the EURAMET MSU using text from the final Publishable Summary.)

2 Need

(Please leave this section blank. This section will be completed by the EURAMET MSU using text from the final Publishable Summary.)

3 Objectives

(Please leave this section blank. This section will be completed by the EURAMET MSU using text from the final Publishable Summary.)

4 Results

This project partially built on previous achievements of EMRP EXL02 SIQUTE and EMPIR 17FUN06 SIQUST projects and went beyond the state of the art by developing optimised single- and entangled-photon sources for quantum metrological application and by demonstrating the quantum advantage achieved by using these sources. In the following, the results obtained for the different objectives will be presented.

4.1 Objective 1

To assess single-photon sources and entangled-photon sources in traceable quantum-enhanced measurements (e.g. quantum calibration at the single-photon level, sub-shot noise measurements, quantum imaging, sub-diffraction imaging and quantum illumination), to overcome classical measurement limits (e.g. noise)

4.1.1 *Executive Summary:*

The project explored new areas of quantum metrology and quantum-enhanced measurements, focusing on single-photon sources (SPSs) and entangled-photon sources in traceable quantum measurements. Key achievements include:

- Development of High-Purity Single-Photon Sources: A high-purity single-photon source (g(2)(0) ~ 0.005) was developed, achieving a record fiber-coupled count rate of nearly 14 Mcps in the telecom range around 1550 nm. A commercial quantum dot (QD)-based source at 927.2 nm was also characterized, showing a high photon flux rate of 17.19 Mphotons/s and a total efficiency of 21.65%, making it one of the brightest sources reported.
- Quantum Microscopy with MIR OPO: A mid-infrared optical parametric oscillator (MIR OPO) setup was developed for quantum microscopy using heralded single photons. It was integrated into a microscope for imaging biological samples and demonstrated suitability for imaging specific biomarkers like lipids and water.
- Calibration of Single-Photon Detectors: A traceable calibration of single-photon avalanche detectors (SPADs) with an uncertainty below 1% was achieved using molecular-doped nanocrystals in polymer microlenses, enhancing durability and photon flux extraction. Calibration was based on the high-purity photon flux from integrated molecule-based single-photon sources under pulsed operation.
- Franson Interferometer Development: An optimized Franson interferometer was developed, achieving 70% visibility in the biexciton-exciton cascade, exceeding the classical limit and violating Bell's inequality. Further optimization included active laser stabilization for improved reliability.
- Efficiency and Source Evaluation: Monte-Carlo simulations suggested that to observe advantages of SPSs over classical sources below the shot noise limit, an overall source efficiency above 40% is needed. Different excitation schemas (non-resonant, quasi-resonant, resonant) demonstrated high single-photon purity with a two-photon probability as low as 0.005.
- Limitations of Entangled Two-Photon Absorption (E2PA): E2PA was found unsuitable for microscopy due to low efficiency, with theoretical calculations indicating limitations from small molecular cross-sections.
- The project advanced quantum metrology by developing high-purity photon sources, innovative detection calibration methods, and new quantum microscopy techniques.

In the following, specific results for the activities focused on in the project with respect to the Assessment of single-photon sources and entangled-photon sources in traceable quantum-enhanced measurements are described in greater detail.

4.1.2 *Validation of a quantum interference mid-IR imaging system for biological imaging.*

In this project, we planned to setup a quantum interference mid-IR imaging system for biological imaging. The system was intended to be based on a non-linear spontaneous parametric down-conversion (SPDC) interferometer setup, which would enable the extension to large wavelength ranges for the probe. Also, it was intended to consider generating microscope imaging (including sub-shot noise imaging, its application to sub-diffraction imaging and quantum illumination). Due to results obtained during the project, especially at the end of the project, the aim of the measurements was changed, see the following sections.

4.1.2.1 Discard of the quantum interference mid-IR imaging system for biological imaging

The quantum interference mid-IR imaging system for biological imaging was discarded due to challenges and limitations encountered during the project. Despite initial experiments, no signals were detected using this technique for biological samples. The system's effectiveness hinges on mid-infrared light interacting with

molecular structures and quantum correlations, but insufficient correlations and low absorption in samples resulted in weak signals. Nonlinear interferometers, though promising for proof-of-concept, are complex to design, maintain, and operate, particularly in biological settings. The technology's sensitivity is highly dependent on various factors, including environmental conditions and signal processing techniques, making it impractical for consistent use. As a result, the project shifted to a more direct absorption method using single MIR photons for imaging, achieving better signal-to-noise ratios without relying on quantum entanglement advancements. This new approach has not impacted the project's overall objectives and is being documented for publication.

4.1.2.2 Summary of the alternative method using up-conversion

We have investigated the noise (STD) of the coincidence measurements, where we find that the noise (STD) of the $g^{(2)}$ function can be minimized when we exactly generate 1 photon per pulse. This indicates the discreetness (quantumness) of the light fields used in our experiment. We find for different rep rates, 10, 20, 40 kHz that the noise is always smallest when we have exactly 0,1,2 photons on average in the pulse. This is not surprising since a photon is the smallest entity of light, thus in the case of 0.5 photon per pulse we will have a superposition of 0 and 1 and in the case of 1.5 photon we will have 1 or 2 photons per pulse. This gives an increase in the noise, which is similar and a typical feature of a thermal state and a signature of entanglement. We are not claiming that this is a witness of entanglement, but just that this feature is very useful for absorption measurements and can be used to measure small absorption features with a better SNR than just using direct measurements. We are claiming that we are projecting 1 photon per pulse (quantum illumination) and using the superposition between 0 and 1 photon for imaging of different samples. We have demonstrated that the source and detection method is suitable for setting up a quantum MIR microscope with quantum illumination. We Investigate small absorption features by imaging polystyrene beads of the size of 20 µm (5 % absorption) and we clearly see that we can resolve the individual beads with a better SNR and resolution using the noise of $g^{(2)}$ than just using direct absorption methods. Currently a manuscript is being drafted about the principle of imaging with noise. This also means the outcome will still be the same, but the technology has changed to a more suitable and useful technology for bio-imaging as described above. Instead of quantum interference measurements we use direct $g^{(2)}$ correlation between signal and idler for imaging. Therefore, quantum interference has been changed to just quantum imaging MIR microscope.

4.1.2.3 Results

The goal of the sub-shot noise experiment was to compare noise levels between a laser and a single-photon source. A semiconductor quantum dot source from Quandela, emitting at 929 nm, was used as the single-photon source, and a PicoQuant laser emitting at 930 nm served as the comparison. Measurements with a superconducting nanowire single-photon detector (SNSPD) showed a count rate of 15 million counts/s for both sources. The results indicated that, for short averaging times (1-10 ms), the single-photon source had a slightly lower noise level than the laser. However, at longer times, the laser showed lower noise. The expected noise suppression of over 3 dB was not achieved, with actual suppression around 0.3 dB, likely due to instability from mechanical vibrations and thermal fluctuations in the single-photon source. The results are depicted in Figure 1.

An entangled-photon source based on SPDC for quantum interference bio-imaging was developed. This involves characterizing the emission spectrum and wavelengths of entangled photons in the near-infrared (NIR) range and measuring probe photon power in the mid-infrared (MIR) range. A cavity-enhanced SPDC, coupled with up-conversion processes, will convert MIR photons to visible and NIR photons, see Figure 2, the parameters are summarized in

Table 1. The SPDC process involves a pump photon at 1064 nm interacting with a nonlinear crystal to produce entangled signal (NIR) and idler (MIR) photons, conserving energy and momentum, and tunable by adjusting the phase-matching condition. The MIR photons can be tuned from 2.9 µm to 4.5 µm. The setup splits the signal and idler photons using a dichroic mirror, directing them to different detectors for imaging and analysis. The study examines the classical correlations between signal and idler photons using a pump rep rate of 20 kHz and measures noise (STD) of coincidence measurements, showing that noise is minimized when exactly 1 photon per pulse is generated. The results align with a Bernoulli distribution, indicating the quantum nature of the light fields. Noise levels are lowest when there are exactly 0, 1, or 2 photons per pulse, a characteristic of entanglement. This feature is valuable for absorption measurements, allowing better signal-to-noise ratios than direct measurements. The results demonstrate the suitability of this source and detection method for quantum MIR microscopy with quantum illumination.

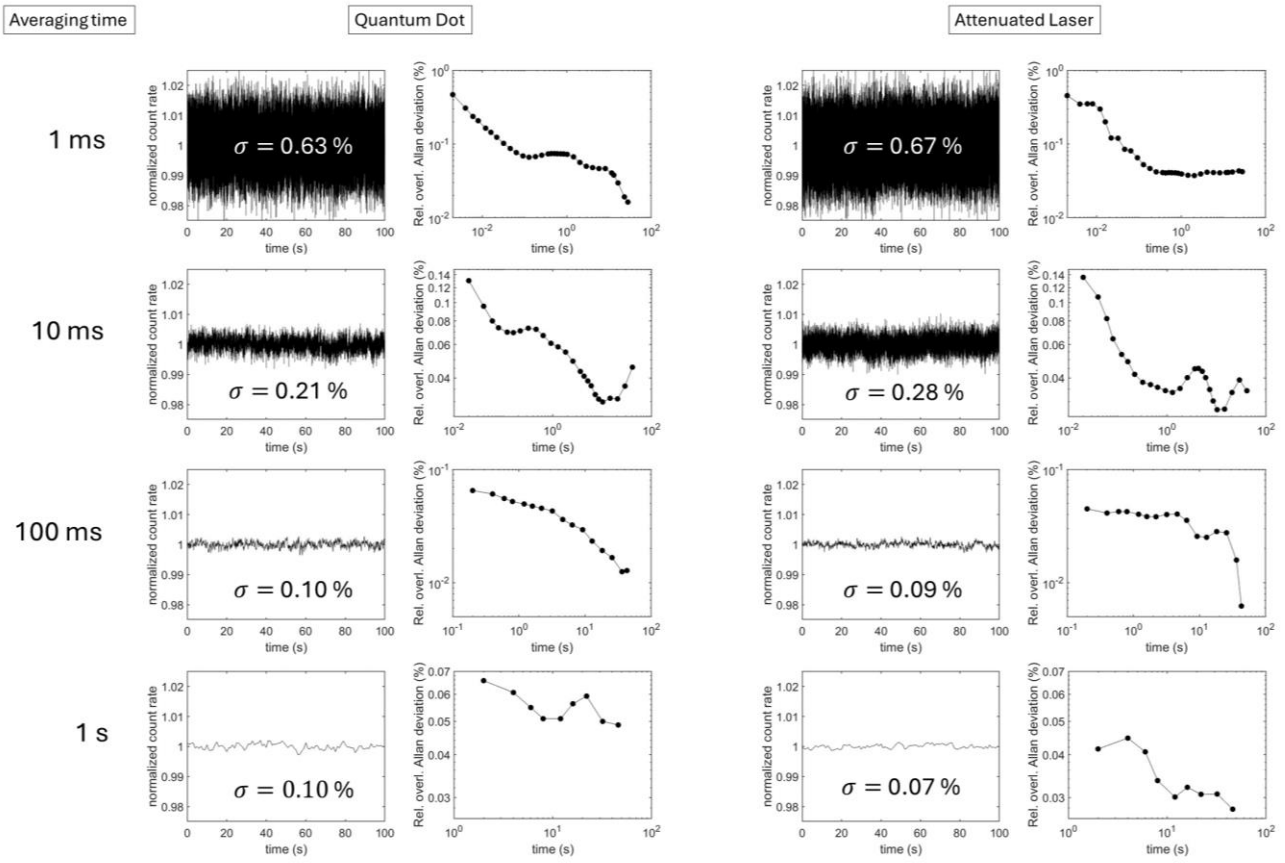

Figure 1: Normalized time traces and relative Allan deviation for two light sources: quantum dot and attenuated laser and four different averaging times: 1 ms, 10 ms, 100 ms and 1 s.

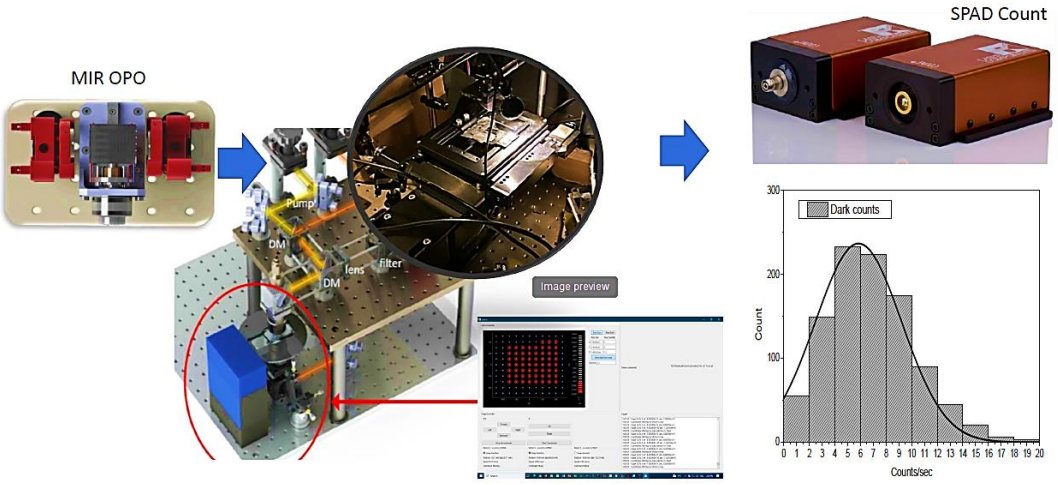

Figure 2: Schematics of the alternative approach for quantum imaging with single MIR photons. The figure shows the main parts of the system, namely the SPDC source, the microscope and the SPADs. The SPADs used have a dark count of approx. 6 cps. The microscope (the xyz stages are from Standa) is controlled by homemade python software and all data is collected with a time-tagger ultra from Swabian.

Table 1: Parameter of the experiment

Emission spectrum and wavelengths of the SPDC generated entangled photons: in the near infrared spectral range: in the mid infrared spectral range:	 NIR ~ 1400-1600 nm -> converted to 610-650 nm MIR ~ 2850 – 4000 nm -> converted to 770 – 830 nm
Power (count rate) of the probe photons in the mid infrared spectral range:	0 – 100 kcps
Normalized g2 between signal and idler (count rate):	0 – 50 kcps

4.1.3 *Application of single-photon and entangled-photon for traceable quantum enhanced measurements*

Next the use of single photons and entangled photons for advanced quantum measurements was investigated, including microscopy and spectroscopy. The focus is on enhancing measurement resolution and reducing noise using techniques like NOON states and quantum illumination, which can achieve sub-shot noise performance. However, the effectiveness of these technologies relies on optimal performance of optical components and photon sources, requiring careful calibration and validation. In the activities mentioned, a Mid-IR quantum interference imaging system for biological samples was developed and needed calibration against classical parameters. Due to challenges, the efforts were limited to quantum imaging MIR microscopy, as quantum interference experiments were not successful.

4.1.3.1 Absorption measurements of polystyrene beads using mid-infrared (MIR) quantum microscopy.

The study first determined the optimal wavelength for these measurements, identifying 3.26 µm as suitable for observing absorption in polystyrene films and beads. Absorption rates are approximately 24 % for a 100 µm thick film, 12 % for 50 µm beads, and 5 % for 20 µm beads. Two wavelengths, 3.26 µm (where absorption occurs) and 2.99 µm (which does not overlap with polystyrene's absorption feature), are used for microscopy and imaging. For demonstrating the MIR single-photon method, 50 µm and 20 µm polystyrene beads are placed on a CaF2 slide, and a raster scan is performed over 3 mm x 3 mm areas at 50 µm resolution. The MIR photons are focused to about 25 µm, and their absorption is monitored using a pump laser at a 20 kHz repetition rate. After passing through the microscope, the MIR photons are converted to visible light and detected with a Single-Photon Avalanche Diode (SPAD). The second-order correlation function ($g^{(2)}$) and photon transmission are measured, revealing absorption features due to scattering and absorption by the beads, see Figure 3.

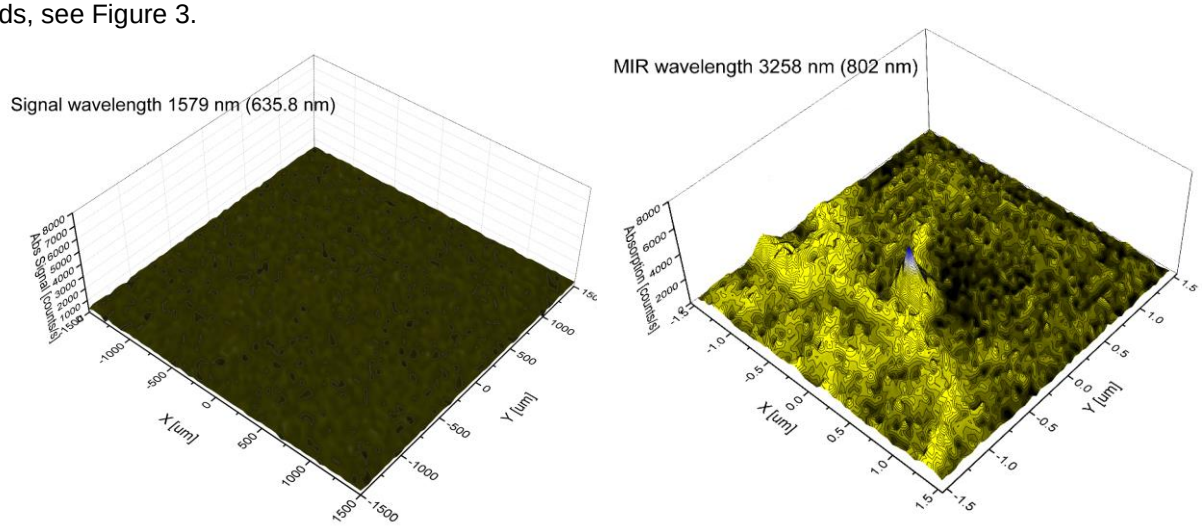

Figure 3: The two figures in the top show absorption maps of the signal and idler photons, while scanning the samples (3x3 mm^2 with 50 µm steps). The signal map is completely flat since the photons are just sent to the SPAD. Each pixel is then used for calculating the g(2) and the noise of the g(2) correlation function. Note that both maps are raw maps no signal processing has been conducted.

In Figure 4, the $g^{(2)}$ function measured at 3.26 µm and 2.99 µm is subtracted to determine the true absorption of polystyrene. While Figure 5 shows the imaging results, the advantage of using $g^{(2)}$ for imaging is subtle; however, the signal-to-noise ratio (SNR) is improved because background photons do not contribute to the imaging. Further investigation focuses on imaging small absorption features in 20 µm beads, showing

improved SNR and resolution compared to direct absorption methods. A manuscript is currently being drafted on the imaging principle with noise.

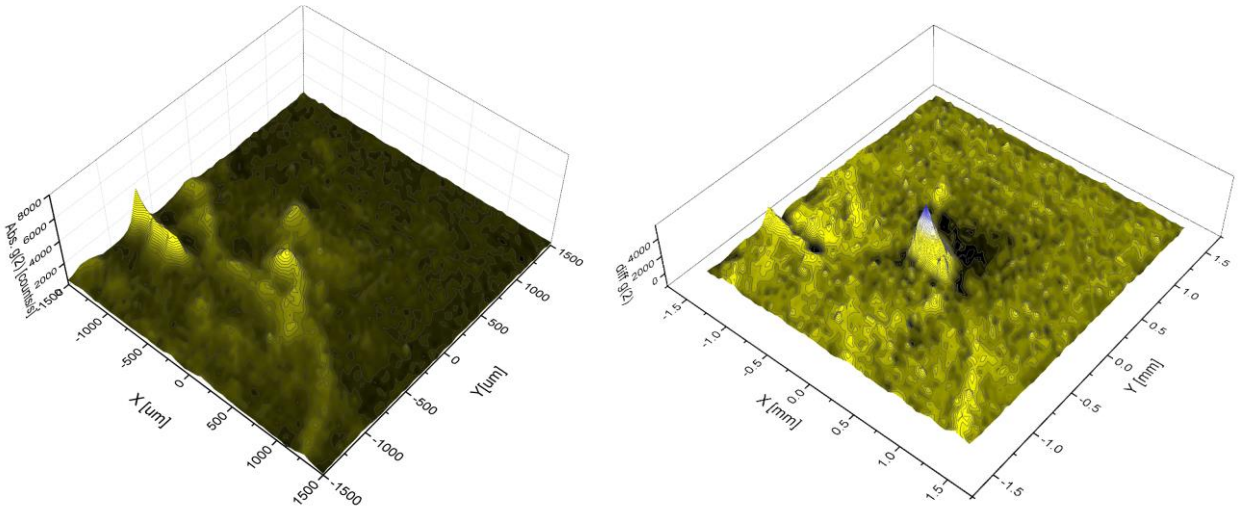

Figure 4: The top figure is the $g^{(2)}$ map at 2.99 µm and bottom is the difference between $g^{(2)}$ at 2.99 µm and 3.26 µm. This map is the absorbance of polystyrene at 3.26 µm.

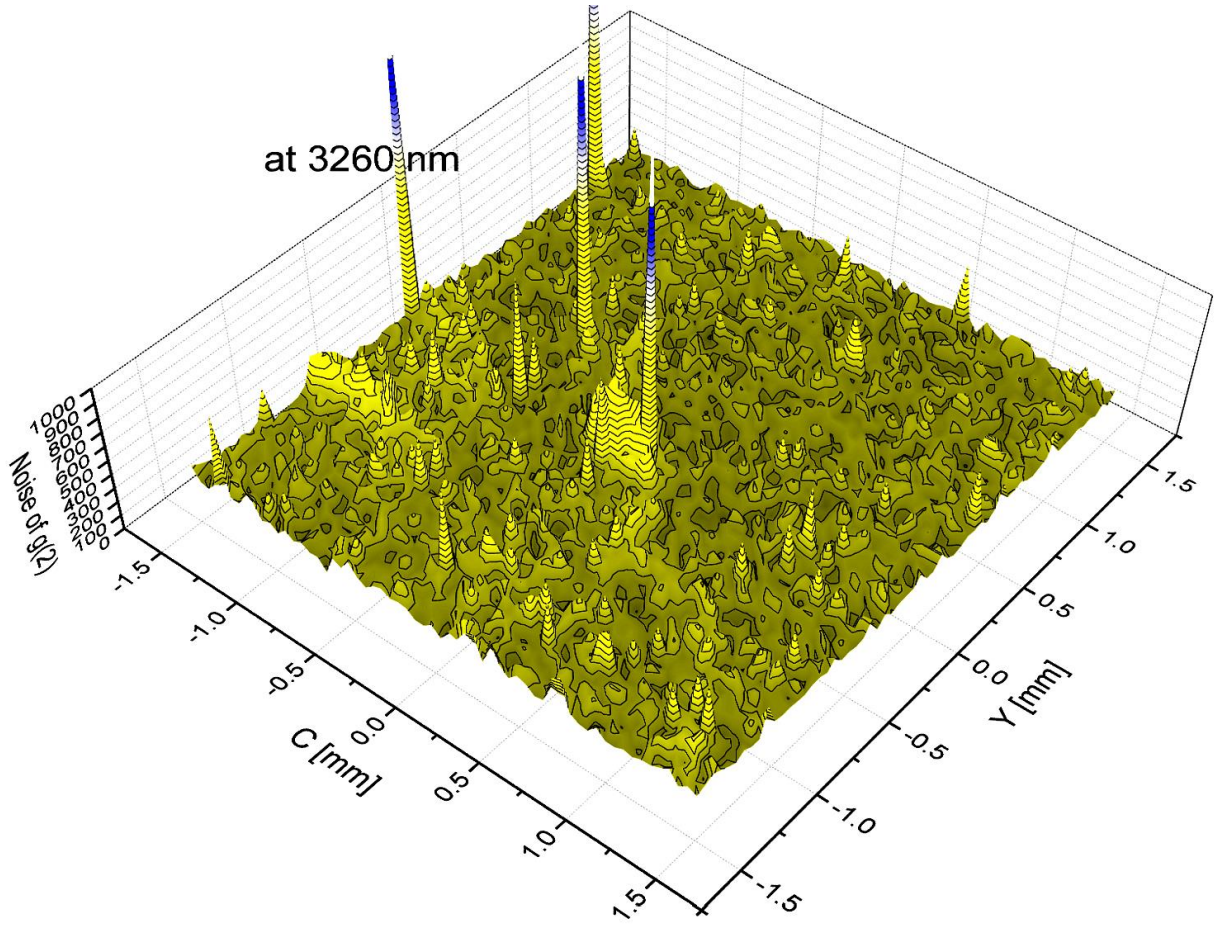

Figure 5: Imaging with $g^{(2)}$ noise. The peaks are due to external noise spikes.

4.1.4 *Single photon based microscopy*

Single photon sources promise to enable a variety of novel quantum technologies, like quantum computing, secure communication via quantum key distribution as well as sensing schemes surpassing the sensitivity of their classical counterparts. Single photon emitters have been proposed as light sources in microscopy due to the different photon statistics from coherent or thermal light sources. Especially for light sensitive samples, which must be examined under low light conditions, the usage of single photon emitters instead of classical sources could be advantageous by reaching uncertainties below the shot-noise limit. To investigate this advantage experiments as well as simulations are conducted comparing the operability of a single photon source and laser source for illumination in a scanning transmission microscope.

4.1.4.1 Experiment

The experiment using a single-photon source based on fluorescence emission from defects in hexagonal boron nitride is described. The emitters are excited in a confocal microscope setup, and their emissions are collected through a single-mode fiber (see Figure 6e). A supercontinuum laser source with a tunable filter is used to cover various excitation energies and compare the single-photon emitter's performance. The emitter's brightness, stability, emission properties, and single-photon purity are analyzed, and its intensity, along with the laser's intensity, is recorded over 30 minutes to calculate the Allan deviation. To test the feasibility of using both sources for microscopy, their emissions are directed into a scanning transmission microscope to image a gold grid on a glass substrate. Light is directed into the microscope via a single-mode fiber, collimated towards the sample, and detected by avalanche photodiodes in a Hanbury-Brown-Twiss (HBT) configuration (Figure 6e). The grid features are 5 µm wide with a 75 µm periodicity. Scans are performed with a 1 µm step size over a 100x100 µm² area. To minimize sample illumination, single events of the laser pulses and detection events on the photodiodes are recorded using a laser repetition rate of 6.5 MHz to keep the data rate within the limits of the time-tagging module. Each pixel is measured for 10 ms, resulting in 65,000 laser pulses per pixel. Post-processing allows for constructing scan images with an arbitrary number of excitation pulses per pixel. Additionally, Monte-Carlo simulations are performed to estimate noise levels of different photon sources at various efficiencies based on different photon statistics.

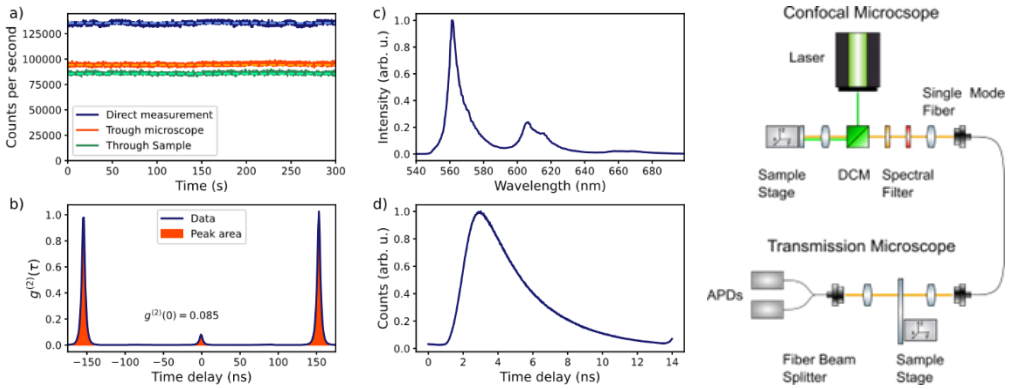

Figure 6: Emitter characterization and experimental setup. a) Count rate measurements under 6.5 MHz excitation measured directly, through the transmission microscope and through the used sample, respectively. b) Second-order autocorrelation measurement for small time delays. c) Emission spectrum of the emitter. d) Recorded lifetime of the excited state. e) Confocal microscope (top) and transmission microscope (bottom) setup.

4.1.4.2 Emitter and setup characterization

A detailed characterization of a single-photon emitter and its application in a microscopy setup is given. The selected emitter, based on defects in hexagonal boron nitride, exhibits high brightness, temporal stability, and a narrow zero-phonon line around 562 nm (Figure 6c). The emitter shows good single-photon purity, with a second-order autocorrelation value $g^{(2)}(0) = 0.085$, corresponding to a single-photon purity of 0.915 (Figure 6b). The setup achieves an average count rate of 130,000 counts per second with an overall efficiency of about 2%, including both collection and detection efficiencies. A transmission of 70% is observed when comparing detected photons from the confocal and transmission microscopes (Figure 6a).

4.1.4.3 Source comparison

For source comparison, the count rates of the emitter and a laser source, both set at 562 nm, are recorded over 30 minutes to calculate their Allan deviations (Figure 7a and b). The laser is attenuated to match the emitter's brightness. Both sources show comparable relative errors for single-pixel durations. The histogram of count rates reveals a symmetric distribution with slight asymmetry due to mechanical drift in the confocal microscope (Figure 7c and d).

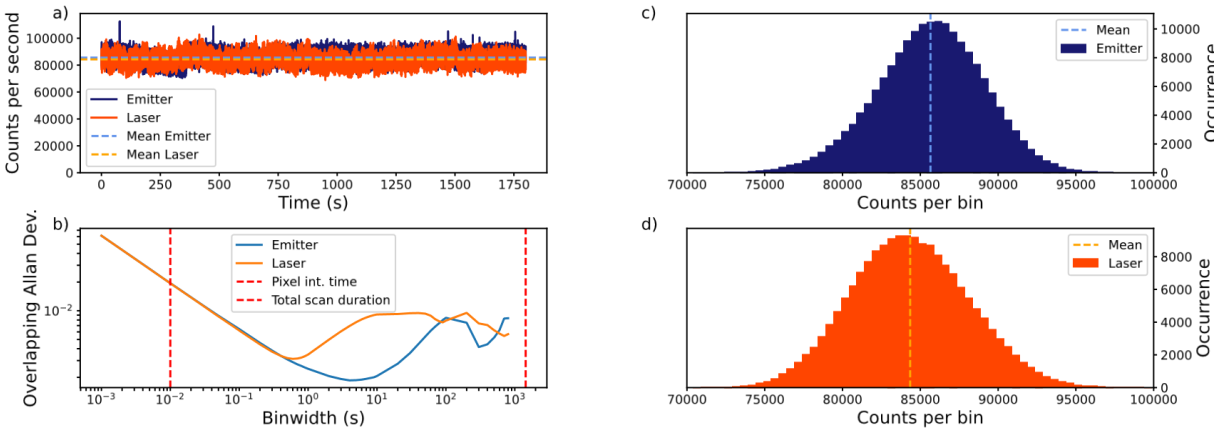

Figure 7: Source and setup characterization. a) Count rates of the emitter and laser through a transmissive point of the sample. The dashed lines indicate their respective mean values. b) Calculated Allan deviation of both sources. The dashed red lines show the measurement duration for a single pixel and the whole scan, respectively. c) and d) Histograms of the occurring photon count rates for both sources.

In scan image analysis, it is demonstrated that as few as 100 laser pulses per pixel can reveal the grid structure (Figure 8b). A more detailed comparison is made with scans using 10,000 laser pulses per pixel. Photon counts in a selected area of constant transmission ((Figure 8c) show mean photon numbers and standard deviations that match expected values ((Figure 8f), indicating that the current source efficiency does not provide a quantum advantage due to the prevalence of empty pulses.

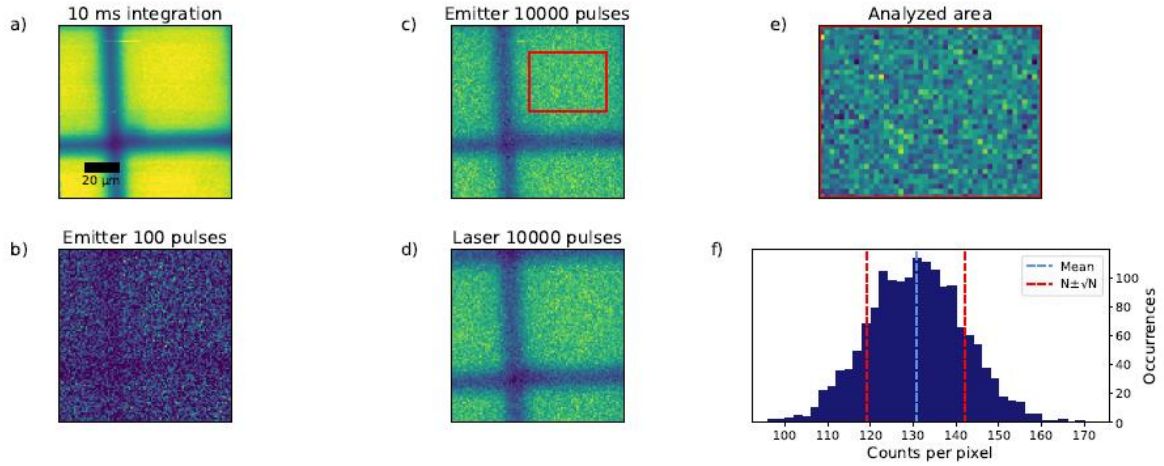

Figure 8: Scan analysis. a) Scan of the STM grid under illumination by the SPE with a total integration time of 10 ms. b) SPE scan with 100 evaluated excitation pulses per pixel. c) and d) SPE and laser scan with 10000 evaluated pulses per pixel. The red rectangle shows an area of constant transmission for further evaluation. e) and f) Closeup of the specified area and histogram of occuring photon numbers in it. The dashed blue and red lines show the mean photon number distances of the square root of it.

4.1.4.4 Simulations

Simulations are conducted to evaluate future experimental requirements, focusing on different source types (thermal, coherent, and quantum emitters) with varying efficiencies and photon statistics (Figure 9a). These simulations suggest that efficiencies of around 30% or higher are required to distinguish significantly between different sources (Figure 9c). The impact of limited photon number resolution on standard deviation is also

assessed (Figure 9e). The influence of emitter contributions to the signal is examined for various source efficiencies, showing that single-photon purity has less impact than source and detection efficiencies (Figure 16f).

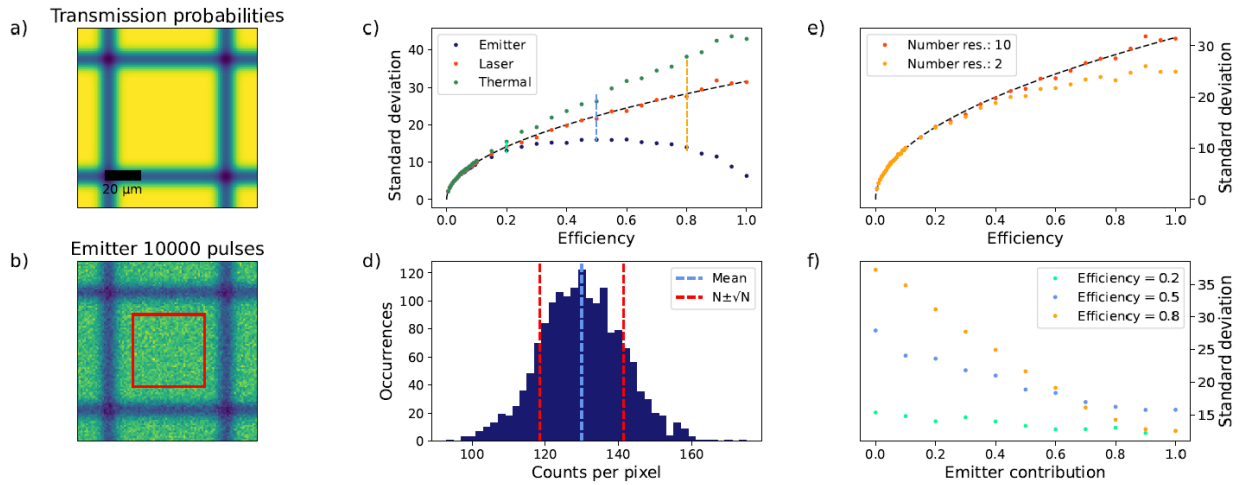

Figure 9: Simulated scan and analysis of different simulated sources. a) and b) Transmission probabilities for different points for the scan and scan for a simulated emitter with 10000 pulses per pixel. The red rectangle indicates the analysis area. d) Histogram of occurring photon numbers. c) Relation between the efficiency and the standard deviations for different sources. The dashed black line shows the square root of the corresponding calculated mean photon numbers. e) Comparison of the standard deviations between number resolution of ten and two for a coherent source. f) Influence of the emitter to background ratio on the standard deviation.

Overall, the experiments and simulations indicate that the current efficiency of the single-photon source is insufficient to demonstrate a quantum advantage, and higher efficiencies are necessary for future experiments to achieve significant differentiation between sources.

4.1.4.5 Conclusion for single photon source-based microscopy

The comparison between a classical source and a single photon emitter for microscopy showed no significant difference. Although both sources were suitable to construct scan images under low light conditions (from as low as a mean photon number of 1.3 per pixel), their standard deviations followed the classical noise expectation. This observation is in good agreement with the conducted simulations, which suggest, that much higher efficiencies are needed (greater than 30 %), including the overall efficiencies of the experimental setup. Furthermore, it was shown that the influence of imperfect number resolution must be considered. Ideally, better number resolution than two is vital to give realistic estimation of noise contributions in future experiments. This becomes more important with higher efficiency.
Based on the results reported, Deliverable 1 aim was achieved and objective 1 aim was partially achieved. We were not able to demonstrate any real quantum advancement for the different technologies, but still showed an advancement using $g^{(2)}$ imaging over direct imaging. The bio-imaging experiment with direct measurement and low flux quantum illumination was achieved, SNR enhancements was achieved in the projection (heralding) of a MIR single photon state for imaging compared to direct measurements of the MIR photons, however, sub-shot noise imaging was not achieved.

4.1.5 *Calibration of an analogue detector using single molecule based single-photon sources, triggered by pulsed excitation*

Within the project, the calibration of an analogue detector using single molecule based single-photon sources, triggered by pulsed excitation, was carried out.

4.1.5.1 Introduction

The development of deterministic single-photon sources (SPSs) is crucial for establishing new standards and metrology procedures. SPSs enable precise exploration of very low optical power levels and the calibration of optical components, such as Single-Photon Avalanche Detectors (SPADs). These detectors often face issues due to photon fluctuations, lack of photon-number resolution, and detector dead time. SPSs, with their sub-

Poissonian statistics, offer solutions to these problems, provided they have bright, pure, and narrowband emissions. Organic molecules are emerging as promising SPSs due to their scalability, portability, narrowband emission, flexible fluorescence wavelengths, and ease of fabrication and operation. This work introduces a new generation of molecular SPSs for quantum radiometry [1], demonstrating improved precision in detector calibration and a model-free approach, surpassing previous methods.

4.1.5.2 Design and fabrication

The calibration of a test detector involves comparing the count rate of a Single-Photon Avalanche Detector (SPAD) with the signal from an analog low-noise reference detector, which is traceable to the national standard for optical radiant flux, the cryogenic radiometer. For accurate calibration, true single-photon pulses must illuminate the SPAD, with intervals longer than the detector's dead time. The design of the single-photon source (SPS) used in this work, along with the optical setup, is shown in Figure 10. The setup integrates sub-micrometric crystals of Anthracene doped with Dibenzoterrylene (DBT:Ac) within Weierstrass-like polymeric microlenses [2], which enhance directionality and photon collection [3], reduce losses at the metal-PVA interface, and provide structural protection across various temperatures. In the experimental setup, single-molecule fluorescence from the zero-phonon line (ZPL) is coupled to a multi-mode fiber and directed either to a fiber-based Hanbury-Brown and Twiss (HBT) setup for purity estimation or to an adaptor sleeve for calibration. Figure 11 shows the data collected for the SPAD calibration.

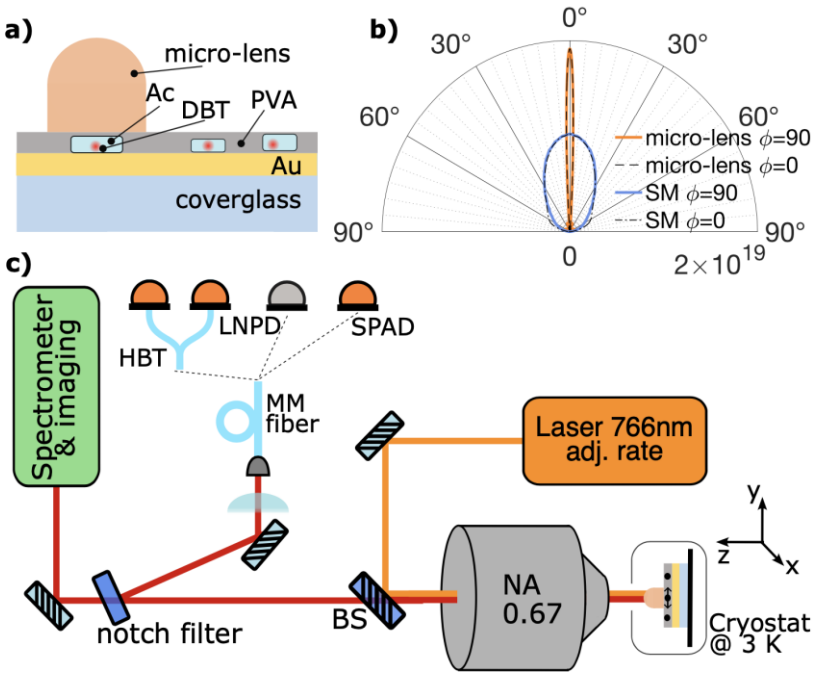

Figure 10: a) Illustration of the structure of the single-photon device. Sub-micrometric crystals of Anthracene (Ac) doped with dibenzoterrylene (DBT) molecules are dispersed on a gold (Au) surface acting as a mirror and are covered with a few hundred-nanometer-thick layer of Poly-Vinyl Alcohol (PVA). The micro-lens fabricated on pre-selected crystals is depicted in orange. b) Angular distribution of the power out-flow for the molecule-based device before and after integration of a micro-lens. c) Sketch of the experimental setup. By means of a notch filter, the molecule emission collected by an epifluorescence microscope is separated in two parts containing the zero-phonon line (ZPL) and the phonon sideband (PSB). Both components can be spectrally analyzed. Additionally, the ZPL component can go through an HBT interferometer to analyze the single-photon purity, or it can be sent to the SPAD or to the analog detector (LNPD) for performing the calibration.

1 P. Lombardi et al., “Advances in quantum metrology with dielectrically structured single photon sources based on molecules”, under review. XXX published!
2 M. Colautti, P. Lombardi, M. Trapuzzano, F. S. Piccioli, S. Pazzagli, B. Tiribilli, S. Nocentini, F. S. Cataliotti, D. S. Wiersma, C. Toninelli, Adv. Quantum Technol. 2020, 3(7), 2000004
3 P. Lombardi, M. Colautti, R. Duquennoy, G. Murtaza, P. Majumder, C. Toninelli, Appl. Phys. Lett. 2021, 118, 204002.

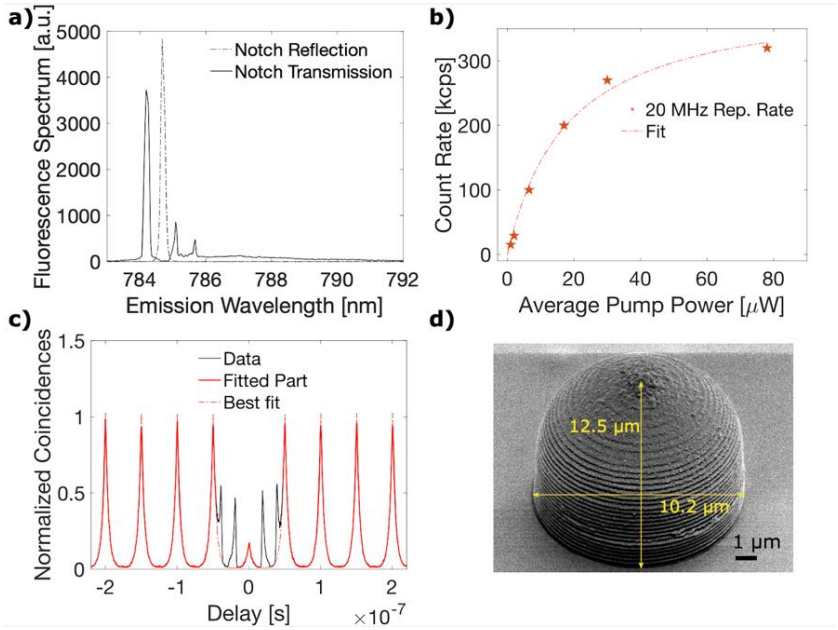

Figure 11: Characterization of the device that was used for the calibration. The measurements in a), b) and c) are taken under 20 MHz pulsed excitation. a) Fluorescence spectrum: solid and dashed lines correspond to the components as separated by the notch filter, transmitted, and reflected, respectively. Each peak belongs to a different molecule. The spectral selection is sufficiently narrow to guarantee collection of photons from a single emitter (at 784.7 nm). b) Count rate detected by the SPAD as a function of the laser pump power. c) Normalized histogram of the inter-photon arrival times for 60 µW average pump power (black solid line). The additional peaks at around 20 ns and 40 ns are due to back-reflections at the flat facets of the multimode fiber components. The red line represents a fit excluding the back-reflections, yielding $g^{(2)}(0)=0.17\pm0.02$. d) Scanning electron microscope image.

4.1.5.3 Detector calibration

The Optics division at PTB hence provided a low noise photodiode (LNPD) traced to the national standard for optical radiant flux and with working range down to few tens of femtowatt which allows for a direct calibration of a SPAD by simply relating the click rate N_{click} to the actual photon flux Φ. As a demonstrative case, we report here the calibration of one of the detectors in use in the HBT setup (Excelitas SPCM-NIR-14, S.N. 37207). To have a proper calibration, correction factors accounting for not ideal behavior of the devices need to be included. According to Refs. [4, 5], these corrections can be introduced in the expression for the evaluation of the quantum efficiency of the SPAD as follows:

$$\eta = \frac{N_{click}}{\phi}\frac{(1-p_A)}{(1-\varepsilon)} \qquad (1)$$

where p_A is the after-pulsing probability for each click event, ε represents the effect due to the probability of having more than one photon per pulse, and the photon flux is determined by means of the LNPD signal U_{LNPD} as

$$\phi = \frac{\lambda}{h\,c}P = \frac{\lambda}{h\,c}\frac{U_{LNPD}}{s_{LNPD}} \qquad (2)$$

where λ/hc is the energy of a photon, P the optical radiant flux estimated by means of the LNPD as U_{LNPD}/s_{LNPD} (corresponding to the signal at the output voltage of the LNPD and the spectral responsivity of the LNPD, respectively). Figure 12a shows the statistical properties of the produced photon stream, where the inset displays a typical count trace from which the flux stability has been evaluated in terms of an Allan deviation (Figure 12a, main panel). The photon flux appears very stable, reaching a relative uncertainty of less than 10^{-3} for integration times of the order of one minute.

To optimize accuracy and precision, the measurements were hence performed as follows: the photon stream is sent to the SPAD and then, immediately after, to the calibrated LNPD; the sequence is terminated by a

[4] H. Georgieva, M. López, H. Hofer, J. Christinck, B. Rodiek, P. Schnauber, A. Kaganskiy, T. Heindel, S. Rodt, S. Reitzenstein, S. Kück, *Metrologia* **2020**, *57*, 055001

[5] H. Georgieva, M. López, H. Hofer, N. Kanold, A. Kaganskiy, S. Rodt, S. Reitzenstein, S. Kück, *Opt. Express* **2021**, *29(15)*, 23500-23507

second measurement with the SPAD. Each step lasts for around one minute, as suggested from the Allan deviation plot. For both detectors, reference level traces are acquired while the signal is delivered to the other device.
Considering Equation 1 and 2, and the procedure described above, the expression used for the calibration becomes:

$$\eta = \frac{h\,c}{\lambda}\, s_{LNPD}\, \frac{(N_{click}^{(1)}+N_{click}^{(2)})/2-N_{DC}}{U-(U_0^{(1)}+U_0^{(2)})/2}\,(1-p_A) \qquad (3)$$

The complete procedure has been repeated for each data point in Figure 12b, where the quantum efficiency of the same device is reported for different photon fluxes and photon source types. We have compared the SPS presented in the previous sections of the paper (pSPS), a similar source operated under continuous wave pumping (cwSPS), and attenuated pulses from the laser used to excite the SPS (pL). We can observe that the value obtained with the pSPS is higher than that obtained from the pL and the cwSPS.

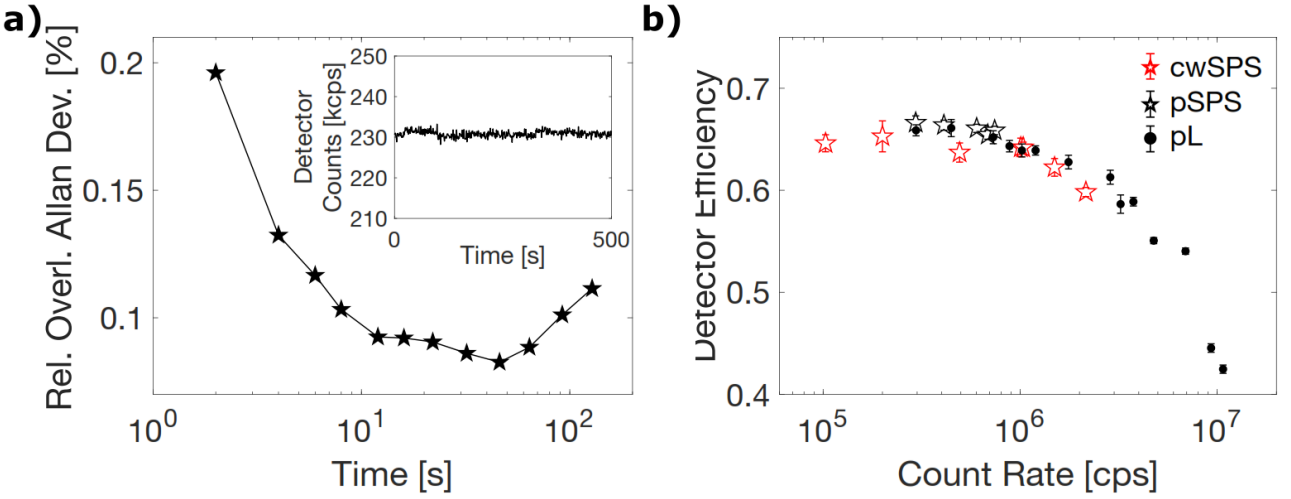

Figure 12: a) Relative overlapping Allan deviation for a laser excitation rate of 20 MHz and an average pump power of 36 µW. The lowest uncertainty is reached for an integration time between 10 s and 50 s. The inset shows the corresponding time trace. b) SPAD detection efficiency obtained from measurements with various source types.

4.1.5.4 Model of the detector response

To extract the intrinsic detector efficiency η_0 from the presented experimental results, a model of the SPAD, following Ref. [6], if we define the click probability per trigger event as q, then N_{click} is determined by q, the detector dead time D and the repetition rate R following the equation

$$R * q = N_{click} + Int[R * D] * q * N_{click}$$

From the equation above, we obtain a general expression for η:

$$\eta = \frac{N_{click}}{\phi} = \frac{R}{\phi}\frac{q}{1+Int[R*D]q} \qquad (4)$$

According to the origin of the photon stream used for the calibration of the detector, the terms in Equation 4 assume different shapes. The specific equations valid for the different illumination sources are summarized in Table 2.

The evaluation of η_0 depends on the type of source. A step-like trend is expected for a pSPS as a function of the repetition rate, regardless of the source efficiency s, as the interphoton time interval is fixed. Differently, a monotonous descending trend characterizes CW sources as the photon flux r is increased. A calibration based on pL shows a combination of both trends. These behaviors are a direct consequence of the probability of photon arrival during the dead times, i.e. the intrinsic non-zero probability of receiving more than one photon within a deadtime interval D at any rate if operating with cwSPS or pL.

[6] H. Georgieva, A. Meda, S. M. F. Raupach, H. Hofer, M. Gramegna, I. P. Degiovanni, M. Genovese, M. López, S. Kück, *Appl. Phys. Lett.* **2021**, *118*, 174002

Table 2: Model functions according to the light source type

Parameter Source Type	ϕ	R*q	Notes	Expression
pulsed Laser (pL)	$R * \mu$	$R(1 - e^{-\mu * \eta_0})$	μ: Poissonian mean photon number	$\eta = \frac{1}{\mu} \frac{(1 - e^{-\mu * \eta_0})}{1 + Int[R * D](1 - e^{-\mu * \eta_0})}$
pulsed SPS (pSPS)	$R * \eta_s$	$R * \eta_s * \eta_0$	η_s: SPS efficiency	$\eta = \eta_0 \frac{1}{1 + Int[R * D]\eta_s * \eta_0}$
cw SPS (cwSPS)	r	$r * \eta_0$	r: photon rate at detector; $Int[R * D]q -> \ r * D * \eta_0$	$\eta = \eta_0 \frac{1}{1 + r * D * \eta_0}$

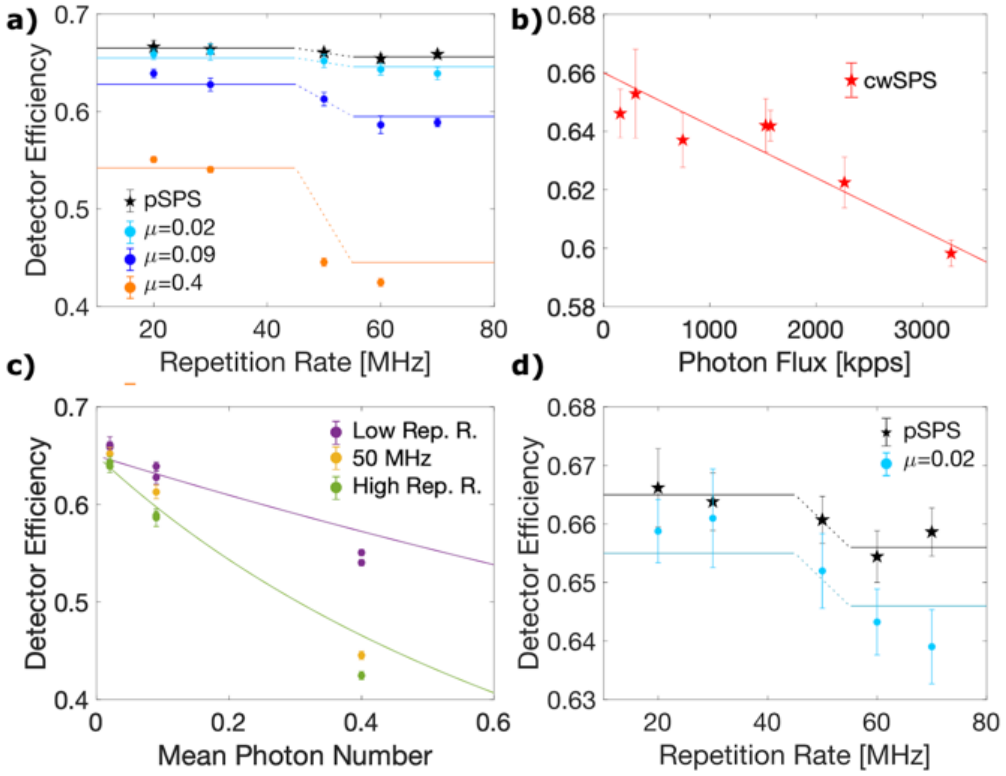

Figure 13: Comparison of the measured data for the detection efficiency – SPSs (stars) and pL (bullets) – with the fitted model functions (solid lines). a) Efficiency as a function of the repetition rate for pSPS and pL. b) Efficiency as a function of the average photon flux for cwSPS. c) Efficiency as a function of the mean photon number for pL, setting η_0 equal to the weighted average of the fitting outputs in a). d) Zoom of the data from a) to compare pSPS and pL for low mean photon numbers.

Figure 13 shows the results of the analysis based on the model presented above, with the estimation of η_0 as best fit to the data for the calibration with the pSPS and the pL (panel a, c and d) and with the cwSPS (panel b). Interestingly, exploiting an SPS under pulsed operation one can benefit from a direct estimation of η_0, without assumption on the model or on the value of the other quantities. Indeed, the "first" step of the vs R curve, where the separation between successive single-photon pulses is longer than the dead time of the SPAD (meaning that Int[R*D] vanishes), exactly yields 0, regardless of any other parameter.

Table 3 summarizes the findings.

Table 3: Intrinsic SPAD Detection efficiency □0 obtained from the calibration with different sources

Source type	pSPS	cwSPS	pL, μ =0.02	pL, μ=0.09	pL, μ=0.4
η_0	0.6650 ± 0.002	0.6600 ± 0.007	0.6590 ± 0.003	0.6470 ± 0.005	0.61 ± 0.01
Relative uncertainty	0.3%	1%	0.5%	0.8%	1.6%

Notably, the calibration reported for the pSPS yields a relative uncertainty of 0.3 % (η_0=0.0665±0.0002), and outperforms the results obtained with the same technique exploiting a quantum dot-based device,[5] despite the higher photon flux achieved in that work. This is probably due to the photo-stability of the molecular sources, combined with the measurement protocol chosen to leverage on it.

4.1.5.5 Conclusions

In this activity, the first calibration of a Single Photon Avalanche Detector using a molecule-based Single-Photon Source under pulsed operation was carried out. The low uncertainty (below 1 %) surpasses other sources, even with higher photon flux. The study demonstrates that pulsed molecule-based single-photon sources can directly estimate detector efficiency without assumptions about source brightness, highlighting its metrological significance.

4.2 Objective 2

To specify the performance parameters of single-photon and entangled-photon sources required to carry out different quantum-enhanced measurements.

4.2.1 *Executive summary*

This project achieved significant progress beyond the state of the art in improving and determining the performance parameters of quantum light sources, focusing on both single-photon sources (SPSs) and entangled-photon sources. Key parameters such as purity, sub-shot noise quantification, entanglement verification, and squeezing measurements for entangled sources, as well as purity, Glauber correlation functions, and photon flux variance measurements for SPSs, were identified and analyzed. These advancements are crucial for various quantum-enhanced measurements and help in characterizing the relevant "quantumness" properties of these sources.

For single-photon sources, a new theoretical model was developed for the emission dynamics of solid-state sources under both pulsed and continuous wave (CW) emission. The model employs second- and higher-order Glauber ($g^{(n)}$) and theta ($\Theta^{(n)}$) parameters to assess non-classical photon emission. The properties of these parameters were investigated for source assessment and are currently being validated against experimental datasets, with findings soon to be submitted for peer review. Furthermore, quantum dot-based SPSs were modeled to optimize parameters such as the Purcell factor and photon extraction efficiency. Various designs, including those for vertical and on-chip extraction and designs with multiple, interfering resonances, were compared and optimized. The methods and scripts developed have been shared through open-access publications.

In the domain of entangled-photon sources, key experimental parameters necessary to evaluate their non-classicality, such as generation probability, decay times, entanglement fidelity, and photon-extraction efficiency, were identified. A quantum state tomography setup was prepared for practical use, enabling detailed assessments of these parameters. It was also established that quantum-enhanced methods relying on Glauber's functions are more robust against losses compared to those depending on outcoupling efficiency, offering significant advantages for certain quantum protocols.

Additionally, the project developed a model for spontaneous parametric down-conversion (SPDC) in various types of nonlinear crystal materials. This model takes into account factors like nonlinearity, phase-matching conditions, and losses, providing insights into parameters such as flux rate, joint spectral amplitude, and purity of the generated photon pairs. A waveguide-integrated photonic cavity was investigated using finite-element modelling, and a surrogate model was developed with machine learning algorithms for design optimization, considering fabrication tolerances. Results and methodologies for these models have also been made available via open-access data publications.

The impact of experimental factors such as dephasing, spectral blinking, and background photons on the non-classical performance of quantum dot-based single-photon sources was extensively studied. It was found that

coherence times below 300 ps significantly reduce visibility, highlighting the importance of maintaining ideal conditions for high-performance quantum light sources. The noise measure, including Von Neumann entropy and Shannon entropy derived from orthogonal POVM measurements, was also estimated, providing further tools for quantifying non-classicality.
Overall, this project has significantly advanced the understanding and development of quantum light sources, providing both theoretical models and practical tools for optimizing their performance for quantum-enhanced measurements.
In the following, specific results for the activities focused on in the project with respect to the performance parameters of single-photon and entangled-photon sources are described in greater detail.

4.2.2 *Identification of Performance Parameters for Quantum-Enhanced Measurements*

In the project, a special focus was on the identification of performance parameters and on the evaluation of noise and inefficiency sources critical for quantum-enhanced measurements using single-photon and entangled-photon sources. The primary goal was to optimize these quantum light sources to enhance their performance in applications such as sub-shot-noise imaging, quantum microscopy, and entanglement tomography.

4.2.2.1 Noise and Inefficiencies in Single-Photon Sources

The concept of non-classicality is a key performance indicator for single-photon sources, particularly in quantum-enhanced measurements. For single-photon sources operating in a pulsed regime, non-classicality is typically characterized by sub-Poissonian emission statistics, observable when measuring over a specific integration time interval. This arises from the source's instantaneous response to repeated excitation pulses under identical conditions [7]. However, these characteristics do not necessarily apply to continuous wave (CW) excitation, therefore the work extended the understanding of non-classicality to single-photon sources operated in the CW regime. In this regime, single-photon emission is modelled as a convolution of two Poisson processes: The excitation process, i.e. a two-level quantum system absorbs a trigger signal (e.g., a pump photon), governed by the reciprocal of the excitation source's optical power and the relaxation process, where the system transitions from the excited state to the ground state, emitting an individual photon, with a characteristic time scale defined by the radiative lifetime of the excited state. Figure 14 illustrates the probability density of photon emission over time for different operation parameters in the CW regime. The analysis shows that non-classicality, marked by sub-Poissonian statistics, is most apparent when the characteristic times of the excitation and relaxation processes are balanced (Figure 15). The non-classical purity, represented by the ε parameter, reaches its optimal value of 0.5 under these conditions. However, when considering optical losses (e.g., outcoupling efficiency and detection efficiency), the non-classicality parameter deteriorates, approaching a value of 1, indicative of a Poissonian system (Figure 16).

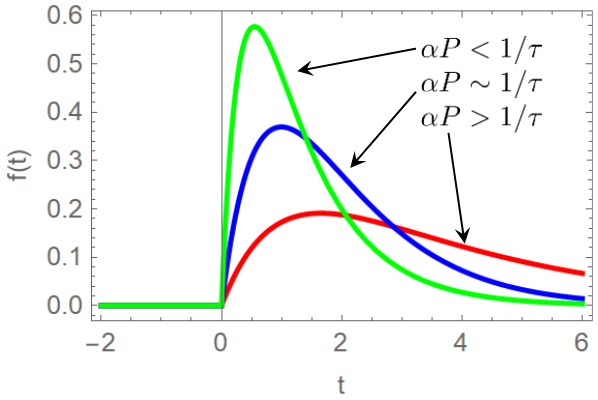

Figure 14: Probability density of photon emission vs. time under different operation parameters in CW regime: $\mu_1 > \mu_2$, $\mu_1 < \mu_2$, and $\mu_1 \sim \mu_2$.

[7] G. Brida et al., "Experimental realization of sub-shot-noise quantum imaging," *Nature Photonics*, 2010.

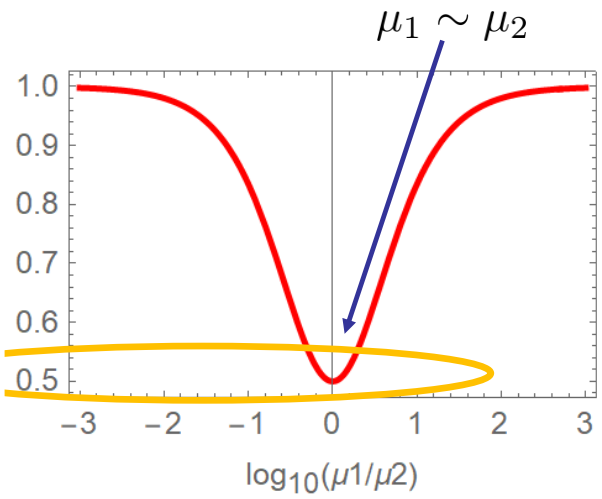

Figure 15: Non-classicality parameter ε as a function of the ratio between the characteristic time scales of the excitation and de-excitation processes.

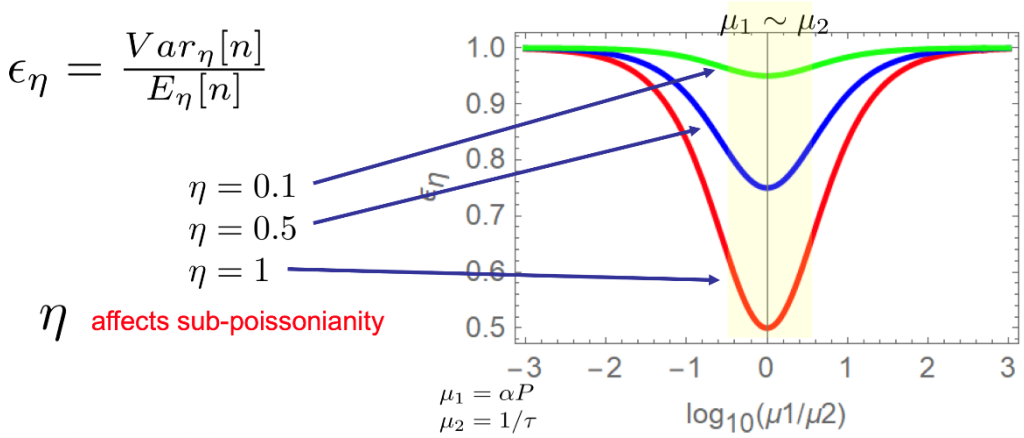

Figure 16: Effects of optical losses h on the non-classicality parameter ε.

4.2.2.1.1 Key Parameters for Single-Photon Source Non-Classicality

The study further investigates the non-classicality of single-photon sources using two classes of quantifiers: N^{th} order Glauber's functions $g^{(N)}(t = 0)$ and $\Theta^{(n)}$ functions. These parameters provide insights into the nature of light sources: The Glauber Functions describe the probability of detecting N-fold coincidences on a detector tree at zero-time delay. The Theta Functions describe the null-coincidence behaviour at zero-time delay. Simultaneous measurement of both parameters allows for more efficient reconstruction of multi-mode light fields, reducing the complexity and effort compared to using either set of parameters alone (Figure 17). Simulations demonstrated that this method could achieve high fidelities above 95 %, even in the presence of noise, making it suitable for detecting non-classical light emissions from fluorescent targets (Figure 18). This study was published in Advanced Quantum Technologies [8].

[8] L. T. Knoll et al., "Photon Statistics Modal Reconstruction by Detected and Undetected Light," *Advanced Quantum Technologies*, 2023.

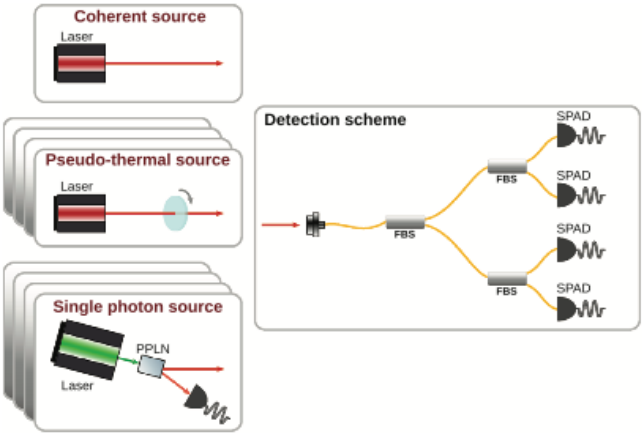

Figure 17: Detection tree for the simultaneous acquisition of the g(N)(t=0) and θ(N)(t=0) parameters

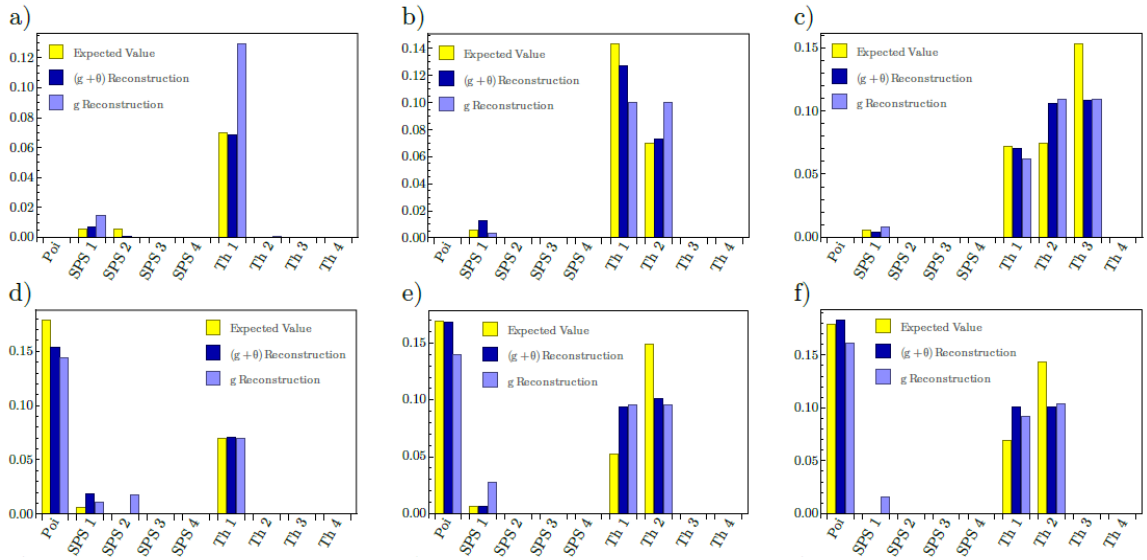

Figure 18: Expected and reconstructed mean photon number per mode for light fields generated by: a) three single-photon emitters; b) two single-photon emitters in the presence of Poissonian light; c) two single-photon emitters together with two thermal fields; d) three single- photon emitters in the presence of a thermal field; e) three single-photon emitters in the presence of a Poissonian field; f) two single-photon emitters with both a Poissonian and a thermal mode.

4.2.2.1.2 Modelling of Quantum Dot-Based Single-Photon Sources

Quantum dot (QD)-based single-photon sources are modelled using two approaches, the Empirical Tight-Binding (ETB) combined with Configuration Interaction (CI), and the combination of CI with the envelope-function k.p. The ETB+CI Model showed better convergence and more accurate results for computing the fine structure splitting (FSS) of quantum dots than the k.p+CI approach (Figure 19). The ETB+CI model, which uses a larger orbital basis, better fits experimental data, particularly for GaAs/AlGaAs QDs, which showed smaller FSS values suitable for entangled photon sources. The project also compared FSS across different quantum dot materials, noting that InAs/GaAs QDs often exhibited larger FSS due to elastic strain from lattice mismatch, making them less ideal for entangled photon sources. Conversely, GaAs/AlGaAs QDs had smaller FSS and were more effective for such applications (Figure 20). Ge QDs on Si substrates showed the smallest FSS, but their indirect bandgap transition made them poor light emitters, limiting their practical use as photon sources.

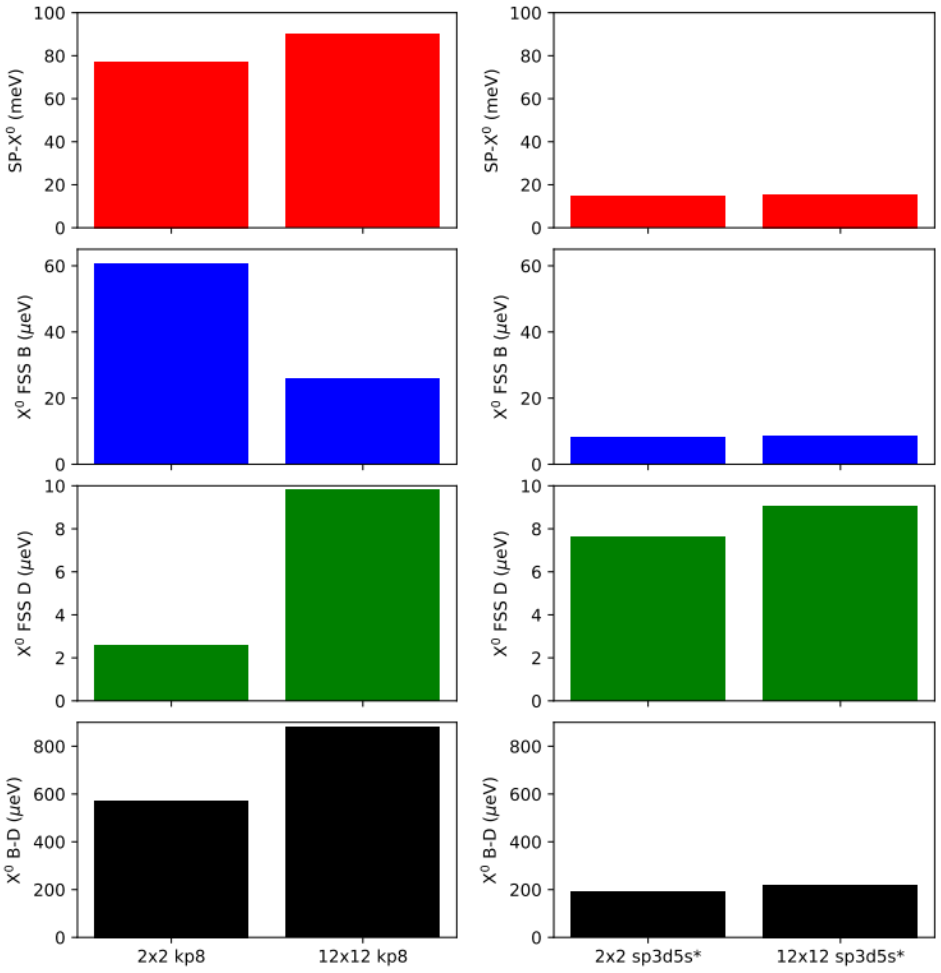

Figure 19: Results of Empirical tight-binding (ETB) computation compared with the results of combination of CI and envelope-function k.p.

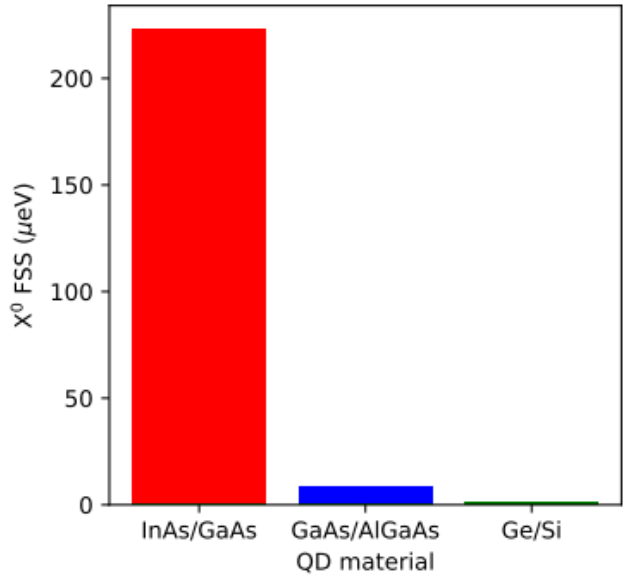

Figure 20: FSS results for different quantum dots configurations.

4.2.2.1.3 Noise Impact on Quantum-Enhanced Microscopy

Within the project, various quantum-enhanced microscopy techniques against real-world noise and inefficiencies were evaluated. The Sub-Shot-Noise Imaging technique relies heavily on the non-classical emission statistics of photon sources. It is significantly affected by losses, especially outcoupling efficiency, which combines quantum efficiency in emission, optical collection efficiency, channel losses, and detection efficiencies. CW-pumped solid-state single-photon emitters have a lower bound on non-classicality at a purity of 0.5, indicating that they are sub-optimal for sub-shot-noise imaging. Pulsed regime sources, despite being affected by optical losses, offer a viable alternative with higher non-classicality [9]. The method of Super-Resolution Imaging uses higher-order Glauber's correlation functions to enhance resolution. These functions are insensitive to detection channel efficiency, allowing super-resolved imaging without significant performance degradation from optical losses. The technique can achieve theoretical resolutions exceeding those obtained with standard methods, especially when combined with structured illumination techniques [10]. Key performance parameters for this application include higher-order Glauber's correlation functions.

4.2.2.2 Noise and Inefficiencies in Entangled Photon Sources

The generation of entangled photon pairs through spontaneous parametric down-conversion (SPDC) and bright squeezed vacuum was examined, focusing on phase-matching and walk-off in nonlinear crystals.
For Spontaneous Parametric Down-Conversion (SPDC), phase-matching conditions are crucial for generating entangled states. The study numerically evaluates joint spectral amplitudes (JSAs) for different phase-matching conditions, such as type II and quasi-phase-matching (QPM), considering real physical parameters (e.g., nonlinearity, mode overlap). The results show that non-collinear SPDC produces a broader spectrum, while collinear propagation is confined to a narrow wavelength band around the phase-matched design wavelength (Figure 21 and Figure 22). The shape of JSAs provides insight into the degree of entanglement. Narrow, anti-diagonally confined JSAs indicate high entanglement, whereas circular JSAs suggest separability (Figure 23). The project revealed that broadband SPDC is more easily achieved using QPM structures due to the longer JSAs, which facilitate better phase-matching.

4.2.2.2.1 Key Parameters for Entangled Photon Sources

Entanglement quality is assessed using negativity as a measure, examining the degree of entanglement in different quantum dot configurations. The study focuses on InGaAs QDs integrated into microlenses, using micro-photoluminescence (μPL) measurements and quantum tomography techniques. Experimentally it was found that μPL spectra and polarization-resolved measurements of QDs show characteristic emission lines corresponding to exciton (X) and biexciton (XX) states. The study also observes photon bunching in different bases, revealing excitonic spin transitions (Figure 24). Quantum tomography further quantifies entanglement by examining polarization cross-correlations, confirming the presence of quantum correlations and the effects of spin precession due to finite FSS. The negativity parameter, derived from the two-photon density matrix, indicates the degree of entanglement. The results show that coherent spin-flip precession does not significantly degrade polarization entanglement if time resolution is high (Figure 24b). However, finite time resolution reduces negativity due to spin precession dynamics.

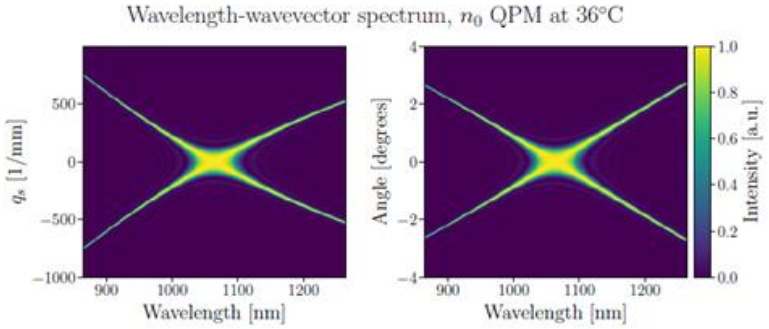

Figure 21: Wavelength-wavevector spectrum for low-gain SPDC assuming quasi phase-matching with 532 and 1064 nm. The spectrum is non-factorizable and clearly illustrates how non-collinear generated waves will propagate at wavelengths far from the phase-matched one.

[9] F. Bouchard et al., Physical Review Applied, 2021.
[10] D. Gatto Monticone et al., Physical Review Letters, 2014.

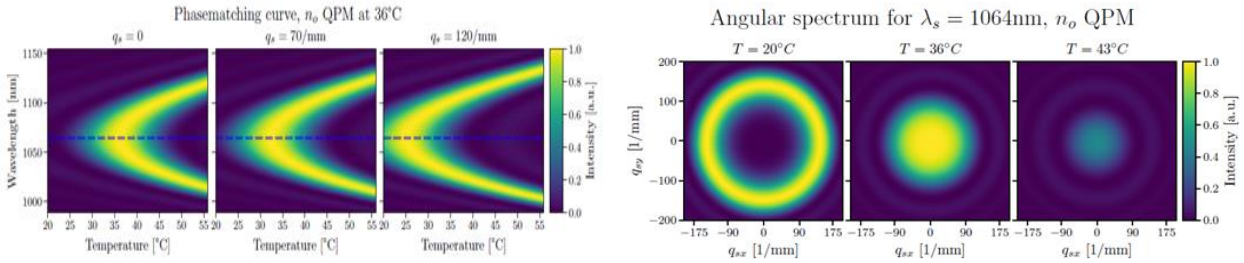

Figure 22: Phase-matching curves for various values of the size of the transverse wavevector. Note in particular how the case for qs = 0 defines a parabola-shaped boundary of wavelengths in the high-temperature region which is inaccessible for all qs. On the other hand, lowering the temperature allows non-collinear photons to phase-match at the degenerate wavelength.

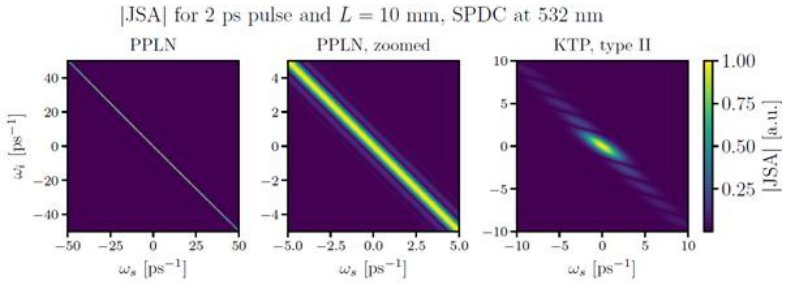

Figure 23: Model of the joint spectral amplitudes for collinear SPDC for 2 ps pulse and 10 mm crystal length.

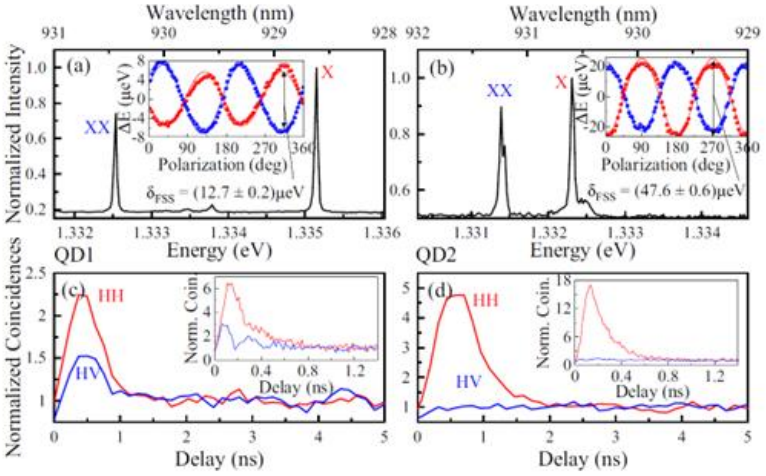

Figure 24: Typical μPL emission spectra of the studied quantum dots (a) QD1 with a FSS of (12.7 ± 0.2) μeV and (b) QD2 with a FSS of (47.6 ± 0.6) μeV. Polarization-resolved measurements of the FSS are displayed in the inset of each graph. Polarization-resolved cross-correlation measurement of (c) QD1 and (d) QD2 in the *HH* basis (red) and in the *HV* basis (blue) obtained with SPCMs with 550 ps temporal resolution. The inset shows the same measurement using SNSPDs with a temporal resolution of 100 ps for comparison.

4.2.2.3 Non-Idealities in Quantum-Enhanced Measurements

The project explored non-idealities in quantum-enhanced measurements using entangled photon sources, focusing on SPDC for two-photon absorption (E2PA). For Two-Photon Absorption Modelling, a numerical tool calculated two-photon absorption probabilities for various quantum states, revealing new dynamics not previously described. The results show that coherent contributions to the two-photon absorption rate scale linearly with photon number at low flux and quadratically at higher flux (Figure 25). This tool helps in understanding complex field-matter interactions and optimizing photon-pair generation.

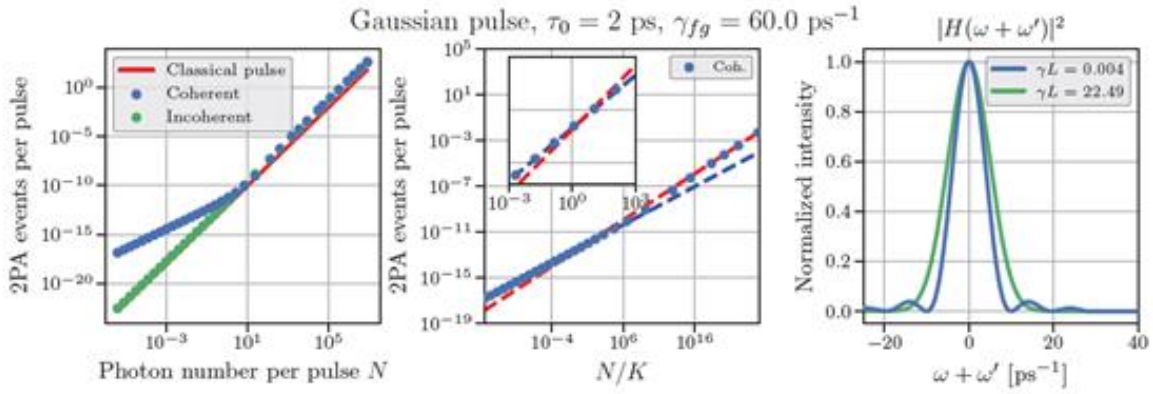

Figure 25: Investigation of the numerically found 2PA rates. For the coherent contributions, we observe a linear scaling with photon number for N/K < 1, with K the effective number of temporal modes. Moreover, we see how the vector H(s), given by the antidiagonal projection of F1 on the transition lineshape, is determined by the spectrum of the SPDC, owing to the broad linewidth of γfg = 60 THz. In this case, the molecule responds instantaneously to the fluctuations of the excitation field.

In conclusion, the project successfully identified critical performance parameters for single-photon and entangled-photon sources required for different quantum-enhanced measurements. It emphasizes the importance of optimizing these parameters to minimize the impact of noise and inefficiencies, thereby improving the performance of quantum technologies in practical applications. The findings highlight the advantages of different quantum light sources for specific applications, providing a clear path for further experimental and theoretical development.

4.3 Objective 2

To develop novel validated methods for the fabrication of single-photon sources and to optimise the sources for highest purity ($g^{(2)}(t = 0)$ close to 0), brightness (photon rate > 5 × 10^6 photons per second) and indistinguishability (Hong-Ou-Mandel visibility > 95 %), according to the performance parameters specified in Objective 2

4.3.1 *Executive summary*

This project made significant advancements in the fabrication and optimization of single-photon sources (SPSs), focusing on achieving high purity, brightness, and indistinguishability. The targets were to achieve a g(2)(t = 0) value of less than 0.001, a photon rate greater than 5 × 10^6 photons per second, and a Hong-Ou-Mandel visibility of over 95%. The project included developing SPSs based on single defects in bulk diamond, single molecules, and InGaAs/GaAs quantum dots (QDs), as well as single and entangled photon sources.
With respect to diamond-based single-photon sources, the project investigated SnV centers in diamond, achieving nearly ideal single-photon emission with g(2)(0) values below 0.1. These centers exhibited narrow resonance lines and stable charge states, which were optimized through annealing at 2100°C and 8 GPa. The charge state of SnV centers was stabilized using blue laser illumination, leading to extremely narrow photoluminescence excitation lines with a cumulative linewidth of 33 MHz, close to the Fourier limit of 25 MHz. A detailed rate equation model including optical ionization to the dark SnV(2-) state was proposed and validated against extensive measurements, confirming that charge-stabilized SnV− centers are nearly ideal in terms of quantum efficiency. The Hong-Ou-Mandel interferometer setup demonstrated single-photon indistinguishability with a classical visibility of over 99.5%. Additionally, GeV color centers were characterized, showing varying single-photon purity (g(2)(0) up to 0.2) depending on the excitation power and achieving a maximum photon flux of 1.2 Mphoton/s. Various ion species (F, Cl, Fe, O, Mg, Mn, Ar, Ge, Pb) were implanted into high-purity single-crystal diamond samples, followed by annealing, to explore alternative emitters.
For quantum dot-based single-photon sources, advanced quantum dot structures, including single-mesa and circular Bragg grating designs, were developed, yielding a record photon flux of up to 14 Mcps and high single-photon purity (g(2)(0) = 0.005) in the telecom C-band. These structures were fabricated using techniques such as in-situ lithography to create monolithic micro-lenses and "Bulls-eye" Bragg cavities around selected QDs. The modified InAs QDs on GaAs substrates achieved linewidths below 40 µeV, fine-structure splitting below

20 µeV, and excellent single-photon purity, indicating the potential for high-performance quantum light sources in the telecom band. Machine learning techniques were employed to improve the position accuracy of QD emitters, enhancing structural quality and brightness. Characterization of single-photon QD emitters at 930 nm and 1550 nm showed spectral characteristics with maximum photon fluxes of 10.99 Mphoton/s and 2.55 × 10^6 photons/s, respectively, with low g(2)(0) values indicating high purity.
As far as molecule-doped nanocrystal single-photon sources are concerned, innovative micro-lens integration on molecule-doped nanocrystals was achieved using direct-laser-writing to fabricate Weierstrass-like polymeric micro-lenses. These integrated micro-lenses enhanced directionality, reduced losses at the metal-polyvinyl alcohol interface, and provided robustness against temperature variations from room temperature to cryogenic levels. By isolating the zero-phonon line (ZPL) of single molecules with a notch filter and spatial selection through fiber coupling, linewidths for DBT systems at 3 Kelvin were kept below 500 MHz. The device demonstrated a photon flux of 300 kcps at the detector with a 20 MHz pump laser, showing a clear anti-bunching feature (g(2)(0) = 0.17 ± 0.02), confirming low multi-photon probability. The limited single-photon purity was mainly due to residual fluorescence from other molecules within the same crystal. The maximum collection efficiency for the micro-dome-integrated molecular source was around 40%, with potential improvements identified for optimized fabrication.
In conclusion, the project achieved significant progress in developing novel methods for fabricating and optimizing single-photon sources across different platforms, including diamond-based centers, quantum dots, and molecule-doped nanocrystals. Advanced fabrication techniques and innovative optimization methods, such as machine learning, were employed to enhance structural quality, brightness, and single-photon purity. These developments set new standards for single-photon source performance, offering significant potential for applications in quantum technologies.
In the following, specific results for the activities focused on in the project with respect to development of novel validated methods for the fabrication of single-photon sources and the optimisation of the sources are described in greater detail.

4.3.2 *Validation of Single-Photon Sources Based on Defects in Diamond and Single Molecules*

Within the project, a detailed validation of various single-photon sources (SPSs) developed using defects in diamond (such as SnV and MgV centers) and single molecules was carried out. The project aimed to develop novel fabrication methods and optimize these sources to achieve high performance in terms of purity ($g^{(2)}(t = 0)$ close to 0), brightness (photon rate > 5 × 10^6 photons per second), and indistinguishability (Hong-Ou-Mandel visibility > 95%). In the following, the progress toward these goals is documented and a thorough characterization of the sources developed, highlighting both achievements and areas needing further improvement are presented.

4.3.2.1 Single-Photon Sources Based on SnV Centres

SnV (tin-vacancy) centers in diamond are recognized for their potential as stable, bright single-photon emitters, particularly suitable for applications requiring indistinguishable photons [11]. These centers benefit from the inversion symmetry of the group-IV vacancy configuration, reducing susceptibility to spectral diffusion caused by fluctuating electrical fields—a common issue with solid-state emitters.
The SnV centers were created by implanting high-purity, single-crystal diamond with Sn ions under various conditions to explore the impact on emitter quality. Two primary samples were studied: one underwent high-pressure high-temperature (HPHT) annealing at 2100°C and 8 GPa, while the other was annealed at 1200°C at ambient pressure for extended periods. The HPHT-treated sample demonstrated superior emitter properties, such as minimal strain, ideal ground state splitting (~820 GHz), and narrow emission lines near the Fourier limit (20-30 MHz) [12]. In contrast, the lower temperature annealing resulted in broader emission lines and increased strain, rendering these samples less suitable for producing indistinguishable single photons.
The SnV centers from the HPHT-treated samples were characterized in detail. At room temperature, they exhibited a characteristic zero-phonon line (ZPL) at 619 nm and a phonon sideband at approximately 660 nm (Figure 26). At cryogenic temperatures (10K), the ZPL became very narrow with minimal phonon sidebands, indicating a high Debye-Waller factor (57%), which is favorable for efficient single-photon emission.

[11] J. Arjona Martinez et al., Phys. Rev. Lett. 129, 173603 (2022).
[12] J. Görlitz et al., New J. Phys. 22, 013048 (2020))

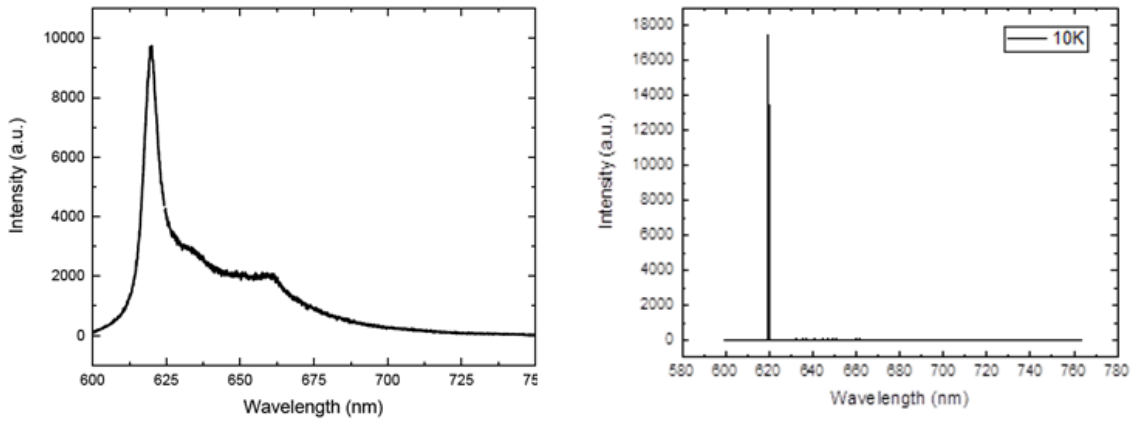

Figure 26: Photoluminescence spectra of a single SnV center at room temperature (left) and 10K (right).

These centers consistently produced pure single photons, with g(2)(0) values below 0.1, where deviations from zero were primarily due to detector dark counts (noise limit g(2)(0) = 0.093). Charge state stabilization was achieved through a controlled illumination process using a blue laser, maintaining narrow photoluminescence excitation (PLE) lines over extended experimental periods (cumulative linewidth of 33 MHz near the Fourier limit of 25 MHz) [13]. A Hong-Ou-Mandel (HOM) interferometer was set up to assess photon indistinguishability, achieving a visibility of over 99.5% under specific conditions. However, further optimization is needed to improve the count rates for resonant excitation setups.
Photonic structures such as diamond nano-pillars were fabricated to enhance photon collection efficiency. These structures, implanted with Sn ions and subsequently annealed, achieved photon count rates exceeding 1 Mcounts/s, a significant improvement over the typical rates in bulk diamond (~200 kcounts/s) (Figure 27).

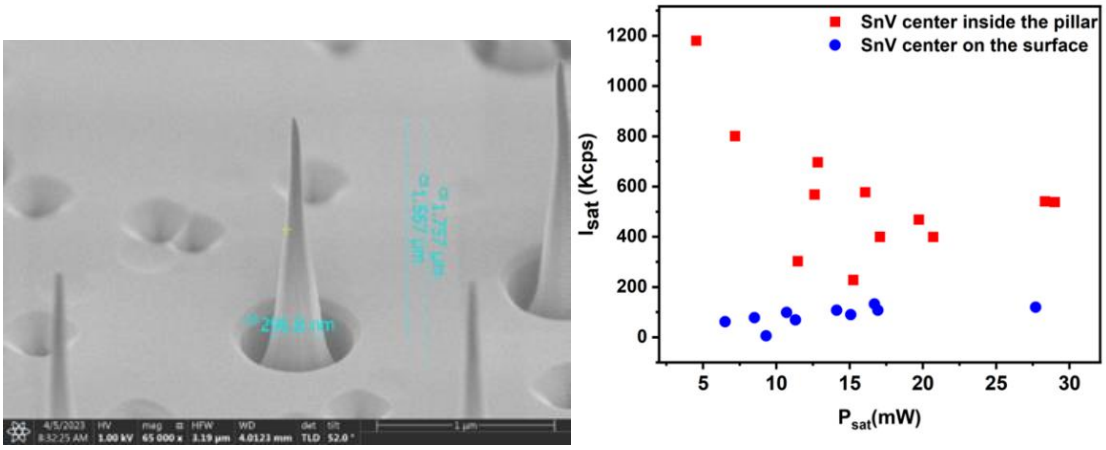

Figure 27: Diamond nano-pillars with implanted SnV centers (left). Saturation count rates and saturation powers of single SnV centers in pillars and in bulk material (right).

4.3.2.2 Single-Photon Sources Based on New Classes of Colour Centres

The search for color centers with optimal emission properties led to exploring new classes of color centers, such as magnesium-vacancy (MgV) centers in diamond [14]. These centers potentially offer advantages like sharp zero-phonon lines and high emission intensity without the extensive lattice distortion associated with heavier group-IV impurities, making fabrication simpler and more reliable.

[13] J. Görlitz et al., NPJ Quant Inf 8, 45 (2022)
[14] E. Corte et al., Magnesium-Vacancy Optical Centers in Diamond, ACS Photonics **2023** 10(1) 101-110

MgV centers were created through ion implantation in diamond, followed by thermal annealing at 1200°C to promote stable, optically active defects. Spectral characterization confirmed the formation of MgV centers, evidenced by a bright zero-phonon line at 567 nm and additional spectral features in the 550-715 nm range. Characterization of MgV centers involved photoluminescence mapping and Hanbury-Brown & Twiss interferometry to assess single-photon emission. The MgV centers demonstrated non-classical emission with $g^{(2)}(t = 0)$ values well below 0.5, indicating high single-photon purity (Figure 28). The radiative lifetime of the excited state was measured to be approximately 2.4 ns, and the photon emission rates varied significantly among different emitters, with maximum rates reaching 1.45 Mcounts/s under optimal conditions (Figure 29).

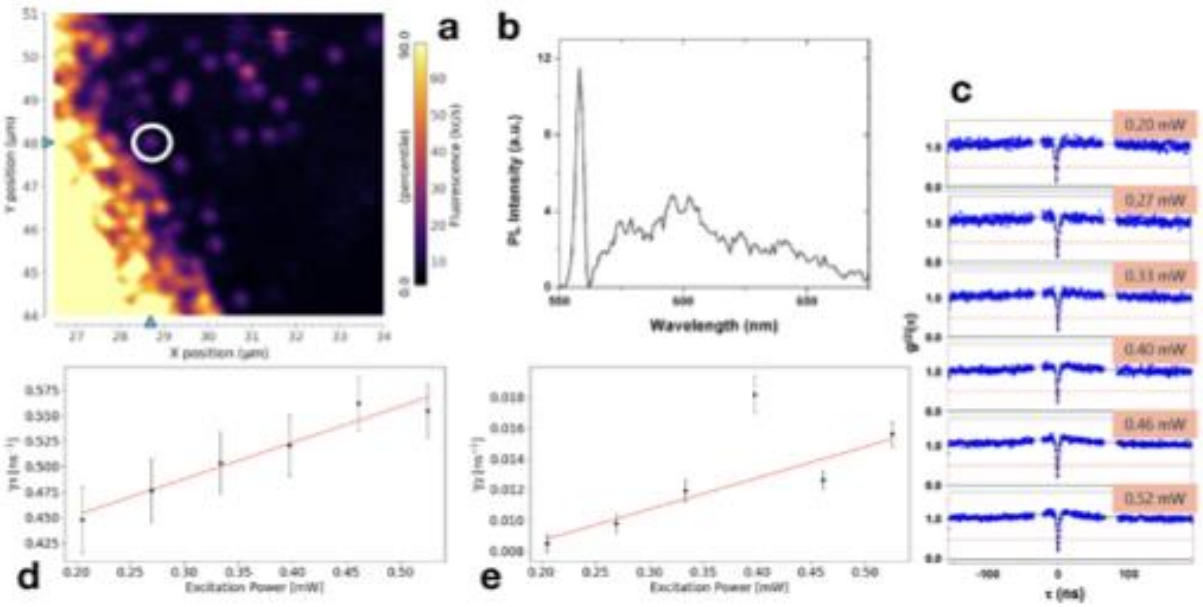

Figure 28: Characterization of MgV centers in diamond. a) PL map of the outer edge of a Mg implanted region. b) PL spectrum of an exemplary MgV single photon emitter. C) $g^{(2)}(t)$ curves acquired at different optical excitation powers. d) and e): dependence of the emission parameters of the 3-level system on the excitation power.

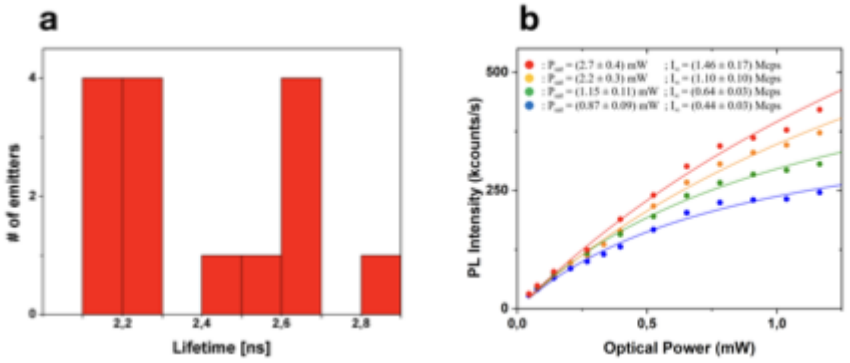

Figure 29: Statistical behavior of 15 individual MgV emitters: a) distribution of the excited state lifetime. b) variability of the emission intensity dependence on the optical excitation power for different, exemplary emitters.

4.3.2.3 Single-Photon Sources Based on Single Molecules

Single molecules, particularly polyaromatic hydrocarbons (PAHs) like Dibenzoterrylene (DBT) embedded in solid matrices, offer promising single-photon emission characteristics, including bright, stable photon fluxes at room temperature and narrowband, highly pure emissions at cryogenic temperatures. These molecules are

particularly suited for applications in quantum radiometry and photonics due to their straightforward integration into polymer photonic structures [15, 16, 17, 18, 19, 20, 21]
Sub-micrometric crystals of Anthracene doped with DBT molecules were dispersed on a gold mirror and encapsulated with a poly-vinyl alcohol (PVA) layer. Micro-lenses were fabricated on selected nanocrystals using direct-laser-writing to enhance emission directionality, reduce losses, and protect the sources against temperature fluctuations (Figure 30). This integrated approach improved photon collection efficiency and overall source robustness.
The single-molecule sources were characterized for their emission spectra, photon flux, and second-order correlation functions. The emission spectra showed distinct lines corresponding to different emitters, and the sources provided photon fluxes up to 300 kcps at a 20 MHz repetition rate (Figure 31). The measured g(2)(0) value of 0.17 ± 0.02 confirmed a low multi-photon probability, suitable for applications requiring high single-photon purity. Additional experiments using a metallo-dielectric antenna structure achieved photon collection efficiencies up to 30%, with photon rates exceeding 6 million photons per second under specific conditions (Figure 32).

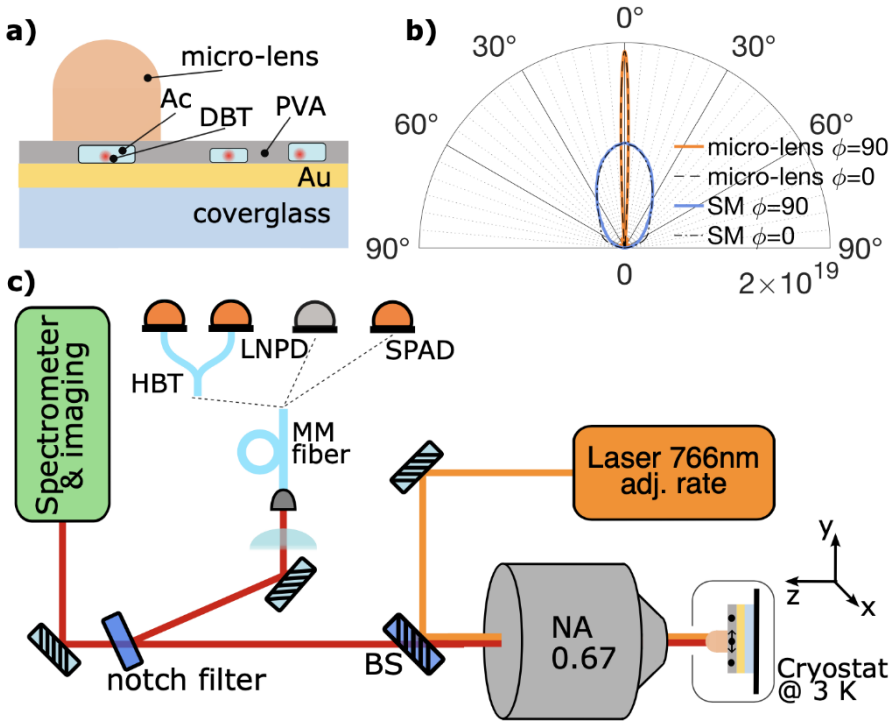

Figure 30: a) Scheme diagram of the SPS design, b) Theoretical emission pattern determined using finite element simulations and b) Experimental setup used for the characterisation of the single-photon emitters.

[15] C. Toninelli et al., Nat. Mat. 2021, 20(12), 1615-1628.
[16] X.-L. Chu et al., Nat. Photon. 2017, 11, 58-62
[17] M. Colautti et al., Adv. Quantum Technol. 2020, 3(7), 2000004
[18] D. Rattenbacher et al., Optica 2023,10(12), 1595-160
[19] P. Lombardi et al., Adv. Quantum Technol. 2020, 3(2), 1900083
[20] P. Lombardi et al., Appl. Phys. Lett. 2021, 118, 204002.
[21] P. Lombardi et al., Advanced Optical Technologies, https://doi.org/10.48550/arXiv.2407.05525.

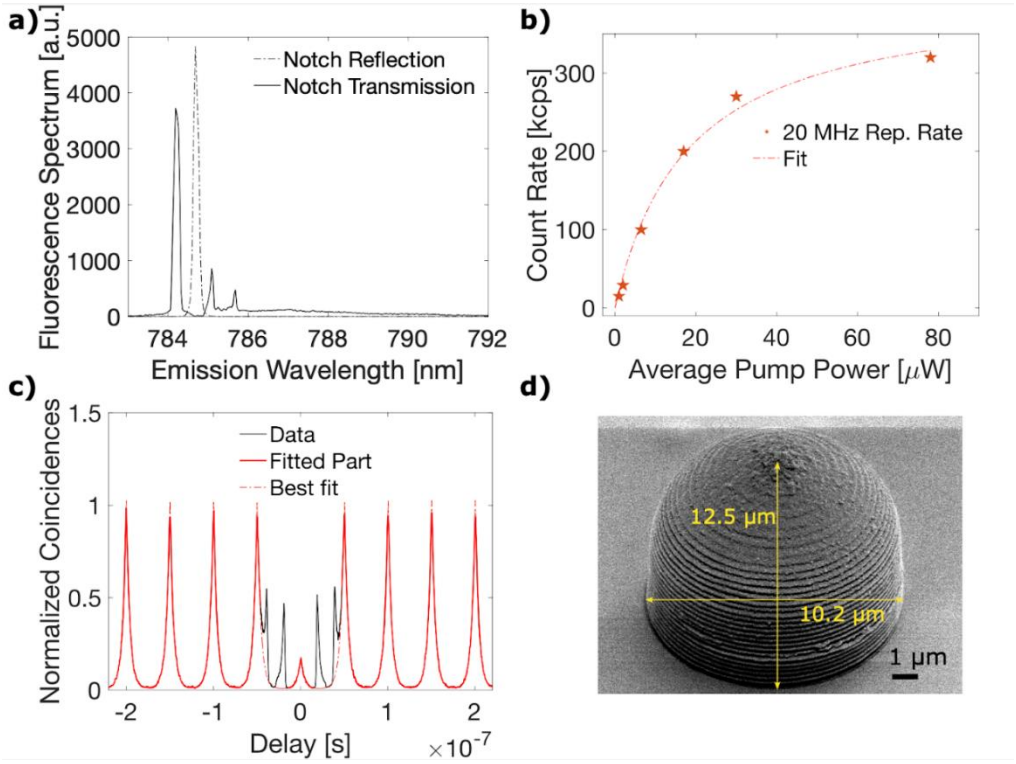

Figure 31: Characterisation of the polymer integrated molecule. a) Emission spectrum, b) Saturation curve, c) Normalized second-order correlation function $g^{(2)}(t)$, d) Scanning electron microscope image of the microlens structure integrating the Sub-micrometric crystals NC.

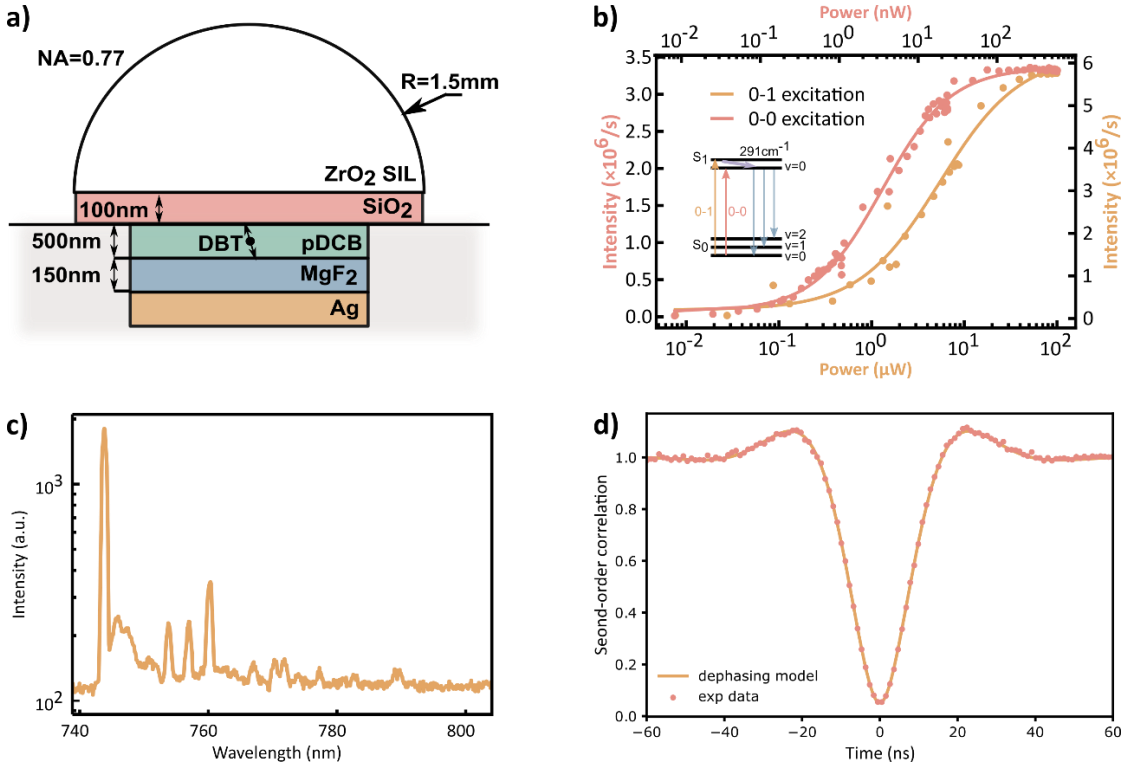

Figure 32: a) Sketch of the metallo-dielectric antenna structure. b) Saturation measurement of two single molecules, one excited via the 0-1 transition (orange) while the second one was excited via the narrow-band 0-0 transition. In both cases the photon detection rates exceeded 10^6 per second. c) Fluorescence spectrum of a single DBT molecule. d) Second-order correlation measurement $g^{(2)}(t)$ of a single DBT molecule inside an antenna.

4.3.2.4 Validation of Single-Photon Sources

In the project, a comprehensive validation of SnV and GeV (germanium-vacancy) centers in diamond, characterised in terms of fluorescence mapping, spectral characteristics, single-photon purity, photon flux, and lifetime were carried out (Figure 33, Figure 34, Figure 35). The GeV centers, enhanced with solid immersion lenses, achieved a maximum photon rate of about 1.2 Mphoton/s with $g^{(2)}(0)$ values below 0.2, demonstrating the potential for high-performance single-photon emission. The findings indicate that while the project made significant progress toward achieving the target specifications, further optimization is required to fully meet all performance objectives.

4.3.2.5 Conclusion

Within the project substantial advancements in the development and optimization of single-photon sources based on defects in diamond and single molecules were achieved. The project successfully fabricated sources with high purity, brightness, and indistinguishability, approaching the desired performance targets. The results provide valuable insights for further improving the fabrication processes and optimizing single-photon source characteristics for quantum technology applications.

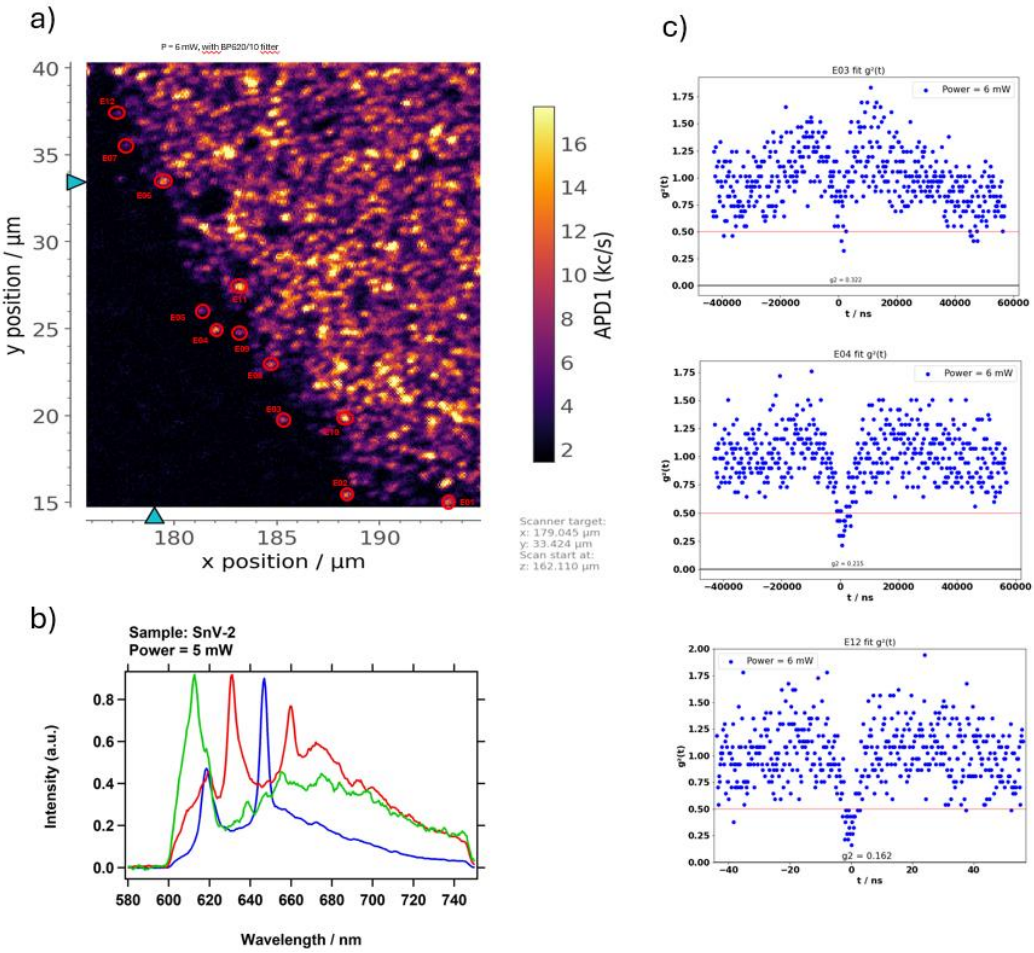

Figure 33: Characterisation of SnV colour centres in a bulk diamond sample. a) Micro-PL, b) Spectral characteristics of selected colour centres and c) Second-order correlation function $g^{(2)}$ (0).

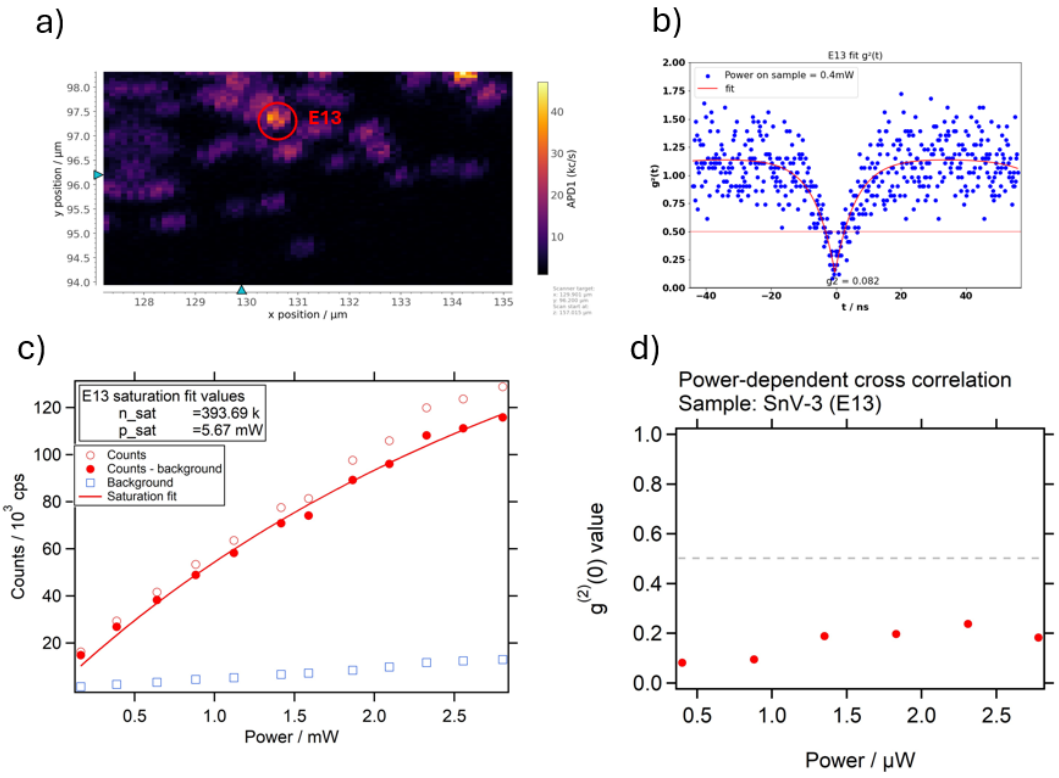

Figure 34: Characterisation of a SnV centre (E13) generated by ion implantation in bulk diamond. a) Micro-PL, b) Second-order correlation function $g^{(2)}(0)$, c) Saturation curve, d) $g^{(2)}(0)$ for different excitation optical powers.

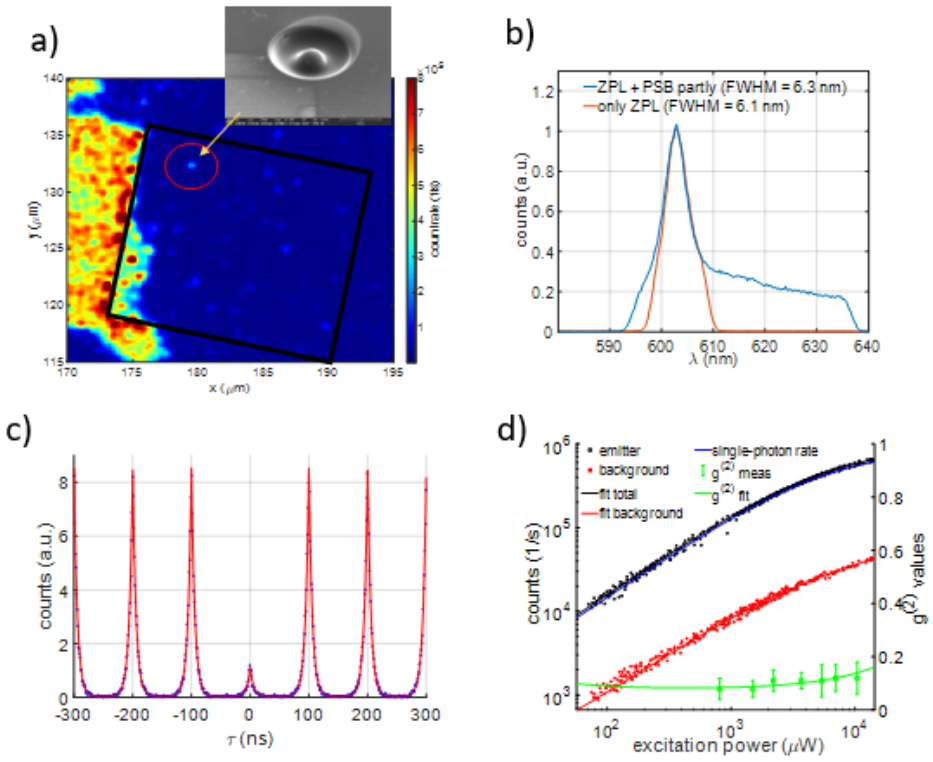

Figure 35: Characterisation of a GeV centre generated by ion implantation in diamond. a) Micro-PL and Semi-hemispherical solid immersion lenses (SILs), b) Spectral characteristic c) Second-order correlation function $g^{(2)}(0)$ and d) $g^{(2)}(0)$ for different excitation optical powers.

4.3.3 *Validation report on the design and fabrication of single-photon sources based on semiconductor quantum dots*

Within the project, the validation of various single-photon sources (SPSs) based on semiconductor quantum dots (QDs), specifically InGaAs/GaAs structures, optimized to achieve the highest single-photon purity, brightness, and indistinguishability was carried put. The project aimed to develop novel fabrication methods and optimize these sources to meet performance goals of a $g^{(2)}(t = 0)$ value close to 0, a photon rate exceeding 25 MHz, and a Hong-Ou-Mandel (HOM) visibility greater than 95%.

4.3.3.1 Single-Photon Sources Based on InGaAs/AlGaAs Emitting in the 910–930 nm Wavelength Range

The development of efficient single-photon sources in the 910-930 nm range was achieved through deterministic in-situ electron-beam lithography (iEBL) processes. This process required transferring the fabrication from an outdated setup to a new machine for reliable and precise patterning, which was delayed due to the pandemic. The focus was on integrating electrically controllable structures with the iEBL process, considering the flexibility required for positioning and contacting quantum dots (QDs) [22, 23].
The design incorporated a combination of a circular Bragg grating structure with a lateral ridge for electrical contacts (Figure 36). This design aimed to maximize photon-extraction efficiency, optimized using full 3D finite-element calculations and Bayesian optimization routines to determine optimal parameters such as layer thicknesses, ring geometry, and etching depth. The initial structures achieved an efficiency of 47% into a numerical aperture of 0.8 (Figure 36) [22, 23].

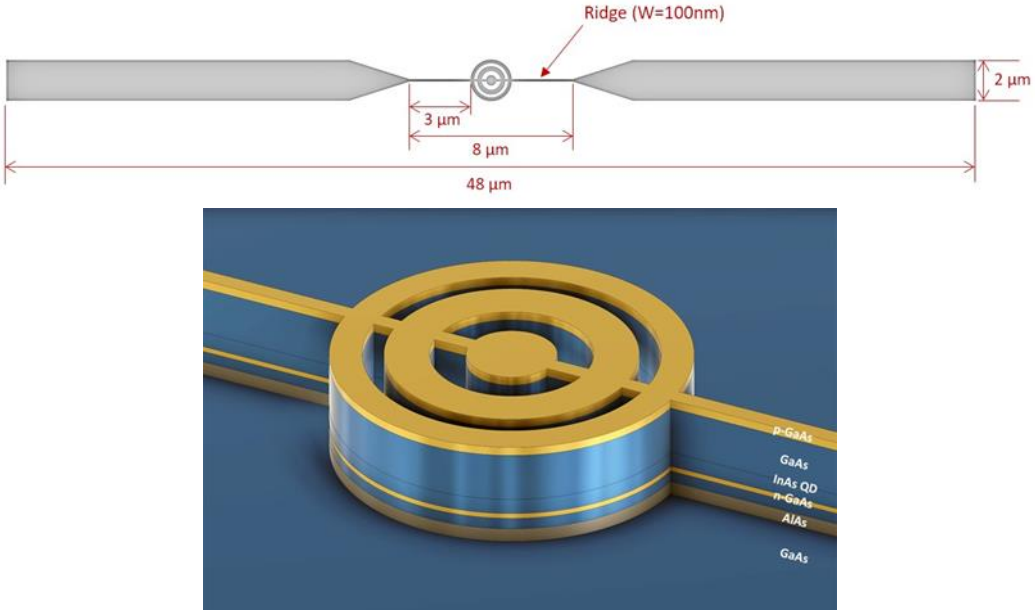

Figure 36: up: Schematic top view of the new SPS structure design for electrically contacted SPSs. The tapered ridges contain doped layers and form the contact paths to the outer, macroscopic contacts. Down: 3D model of the nanophotonic structure with naming of the integrated layers that were optimized by full 3D calculations.

Characterization included micro-photoluminescence (µPL) measurements under varying bias voltages, showing fine spectral tuning and control over different excitonic complexes (Figure 37). The single-photon purity was evaluated using Hanbury-Brown and Twiss measurements, resulting in a $g^{(2)}(0)$ value of 0.06, demonstrating a high level of single-photon emission (Figure 38). Indistinguishability was assessed through Hong-Ou-Mandel (HOM) measurements, yielding a non-post-selected visibility of 25.8% and a post-selected visibility of 92.8% (Figure 39) [22, 23].

[22] L. Bremer et al., Optics Express 30, 15913 (2022)
[23] L. Rickert et al., Optics Express 31, 14750 (2023)

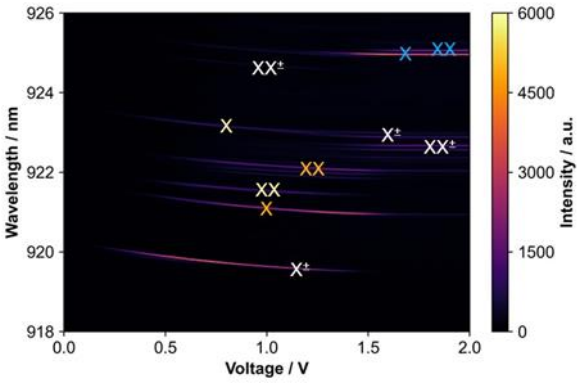

Figure 37: Measurement of the emission of three QPs in an electrically contacted SPS structure using µPL and as a function of the applied bias voltage. A clear blue shift (smaller wavelengths) can be seen, indicating that the internal diode field is compensated by the applied voltage. Also, a switching on and off of different excitonic complexes is observable. The identification of the excitonic complexes is based on polarization and power dependent measurements.

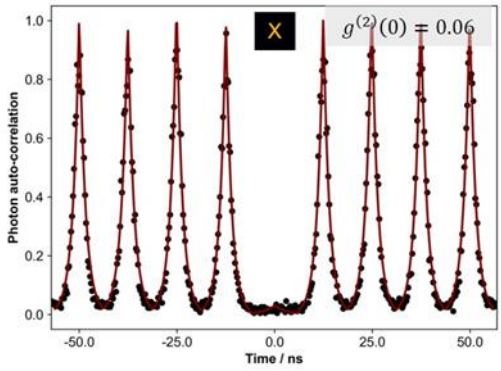

Figure 38: $g^{(2)}(t)$ -correlation histogram measured at the orange X-line in Figure 37. The almost vanishing $g^{(2)}(t=0\ \text{ns})$ value of 0.06 proves the high quantum optical quality of the newly developed SPS diode structure.

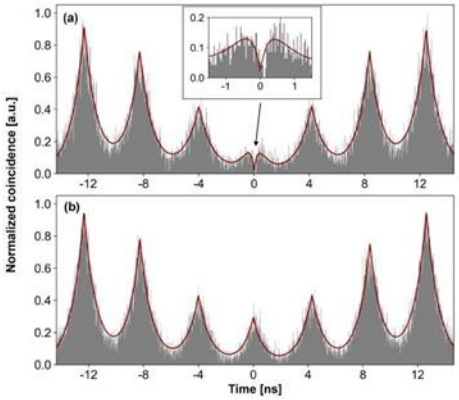

Figure 39: The Hong-Ou-Mandel statistics $g^{(2)}(t)$ of the X state of the SPS biased at 1.3 V for parallel (a) and orthogonal (b) polarization. A non-post-selected visibility (V_{raw}) of (25.8 ± 2.1)% and a post-selected visibility (V_{post}) of (92.8 ± 4.8)% were determined.

4.3.3.2 Single-Photon Sources Based on InGaAs/AlGaAs Quantum Dots Driven by Electrical Means

This section focuses on single-photon sources driven and tuned independently by electrical means. The design incorporated new nanophotonic antennas compatible with an electro-optical pumping scheme, using Mie-Tamm and surface-plasmon optical modes to enhance brightness and collection efficiency (Figure 40) [24].

[24] J.M. Llorens and B. Alén „Inverse Design of a Hybrid Mie-Tamm Photonic Structure as a Highly Directional Gigahertz Single-Photon Source“, Phys. Rev. Applied 19, 034054 (2023).

The photonic structures were fabricated through a process involving epitaxial growth, definition of metallic nanodisks by electron-beam lithography, and a series of etching and deposition steps to create a hybrid Mie-Tamm cavity. Challenges such as sidewall roughness and the need for planarization were identified, suggesting further refinement in fabrication methods (Figure 41) [24].
Characterization revealed that the fabricated structures did not consistently meet the nominal parameters required for optimal single-photon emission. However, some individual micropillars showed promising characteristics, with time-resolved micro-PL measurements indicating typical InGaAs QD radiative recombination lifetimes and some enhancement in collection efficiency under specific conditions (Figure 42, Figure 43) [24].

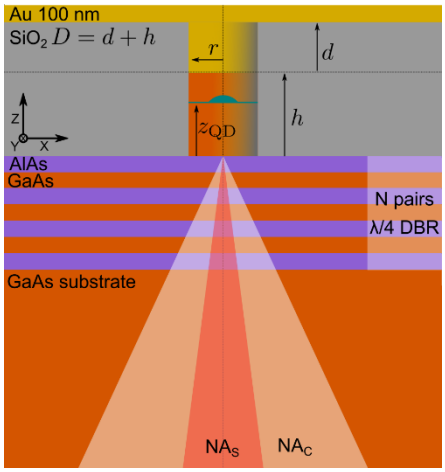

Figure 40: Hybrid Mie-Tamm photonic design.

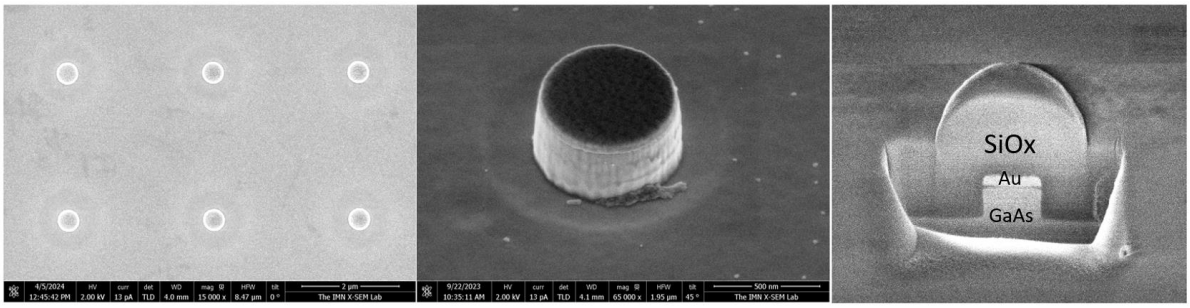

Figure 41: SEM Images of fabricated structures.

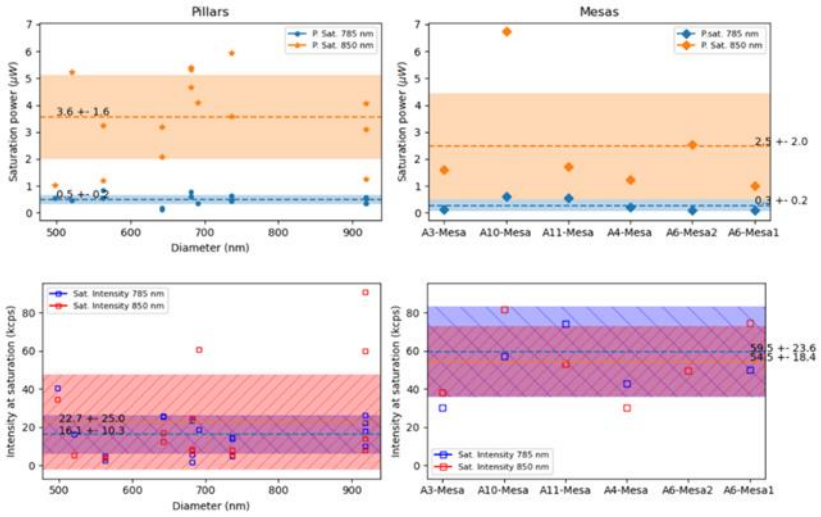

Figure 42: Emission saturation characteristics of individual micropillars and individual QD on mesas.

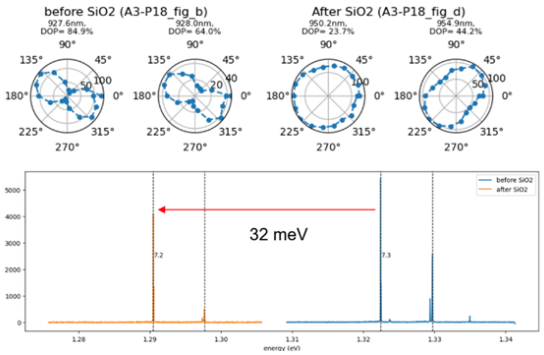

Figure 43: Emission characteristics before and after SiOx deposition.

4.3.3.3 Single-Photon Sources Based on In(Ga)As Emitting at 1550 nm

Single-photon sources emitting in the 1550 nm wavelength range are crucial for applications in quantum technologies due to their compatibility with telecom C-band transmission, which allows for low-loss transmission through both atmospheric and fiber optic mediums. The development focused on reducing strain through a metamorphic buffer (MMB) approach and optimizing the design for incorporation into photonic structures such as circular Bragg grating (CBG) cavities [25, 26, 27, 28, 29, 30, 31, 32, 33, 34]. The MMB design involved optimizing strain reduction while maintaining a smooth surface suitable for processing techniques and efficient integration into a λ-cavity. A jump-convex-inverse grading profile was adopted to maximize strain relaxation without inducing unwanted 3D growth (Figure 44, Figure 45, Figure 46] [35, 36, 37, 38, 39, 40, 41, 42]. Photoluminescence spectra confirmed the emission characteristics, showing a stable growth process with minimal wavelength variation despite changes in indium content. The QD emission peaks were consistently observed around 1550 nm, with optimization leading to improved single-photon emission rates.

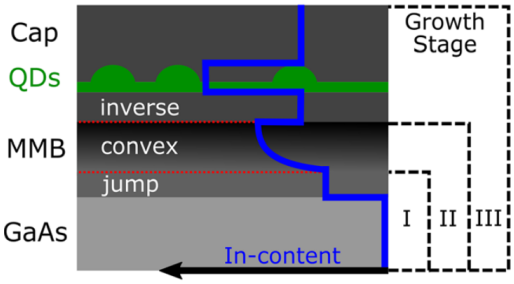

Figure 44: Schematic structure of InAs QDs inside an InGaAs-matrix lattice matched to an MMB grown on a GaAs substrate. The varying indium content throughout the structure is illustrated in blue. Growth optimization is performed in three consecutive growth stages I, II and III. [36]

[25] P. Michler, Quantum Dots for Quantum Information Technologies, Volume 237. Springer, (2017).
[26] S.-K. Liao et al., Nature Photonics, 11(8):509–513, (2017).
[27] G.P. Agrawal. Fiber-optic communication systems, volume 222., John Wiley & Sons, (2012).
[28] K. Takemoto et al., Japanese journal of applied physics, 43(3A):L349, (2004).
[29] N.N. Ledentsov et al., Journal of crystal growth, 301:914–922, (2007).
[30] M. Paul et al., Applied Physics Letters, 111, 33102, (2017).
[31] K. D. Zeuner et al., ACS Photonics 8, 2337–2344, (2021).
[32] C. Nawrath et al., Applied Physics Letters 115, 023103, (2019).
[33] C. Nawrath et al., Advanced Quantum Technologies 6, 2300111 (2023).
[34] J. Liu et al., Nature Nanotechnology 14, 586–593 (2019).
[35] M. Paul, et al., Applied Physics Letters 111, 033102 (2017).
[36] R. Sittig, et al., Nanophotonics 11, 1109 (2022).
[37] A. Andrews, et al., Journal of Applied Physics 91, 1933−1943 (2002).
[38] B. Rodriguez et al., Journal of Crystal Growth 264, 64−69 (2004).
[39] T. Sasaki et al., Journal of Crystal Growth 323, 13-16 (2011).
[40] S. DenBaars et al., Journal of Crystal Growth 77, 188 – 193 (1986).
[41] A. M. Ceschin et al., Journal of Crystal Growth 114, 693 -699 (1991).
[42] L. Sapienza, et al., Nature Communication 6, 7833 (2015).

Further integration into CBG cavities was planned to enhance brightness and Purcell factors, with simulations showing promising enhancements (Figure 47, Figure 48, Figure 49) [43, 44, 45, 46, 47, 48, 49, 50, 51, 52, 53, 54, 55]. The CBG devices demonstrated high collection efficiencies and a maximum Purcell factor of 16.6, aligning well with simulation predictions. Time-correlated single-photon counting (TCSPC) measurements showed a decay time of 0.52 ns, yielding a Purcell factor of 3.0. Single-photon purity was measured with $g^{(2)}(0)$ values as low as 0.0072 under specific conditions, demonstrating the high performance and suitability of these sources for quantum communication applications (Figure 50, Figure 51) [43 - 55].

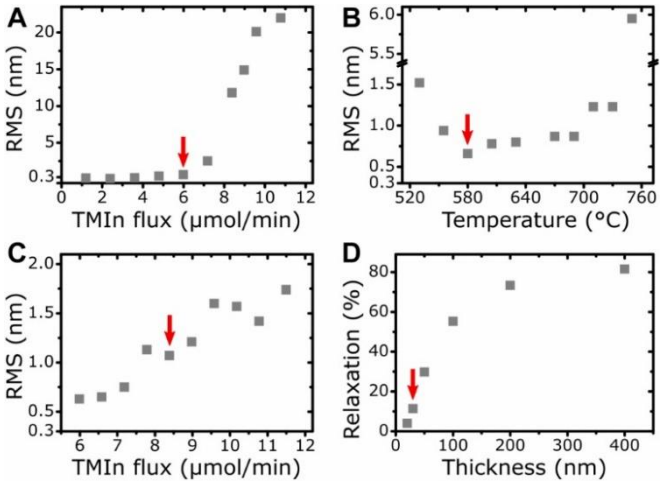

Figure 45: Successive optimization steps of growth stage I. The red arrows mark the obtained parameter values. (A–C) RMS surface roughness of InGaAs layers with varying growth parameters. (A) Variation of TMIn flux for the growth of 50 nm InGaAs with 20.8 µmol/min TMGa flux and 2973 µmol/min AsH_3 flux at 710 °C. (B) Temperature dependence of InGaAs with a TMIn flux of 6.0 µmol/min. (C) Variation of TMIn flux at 580 °C. (D) Strain relaxation of $In_{0.274}GaAs$ depending on layer thickness. [36]

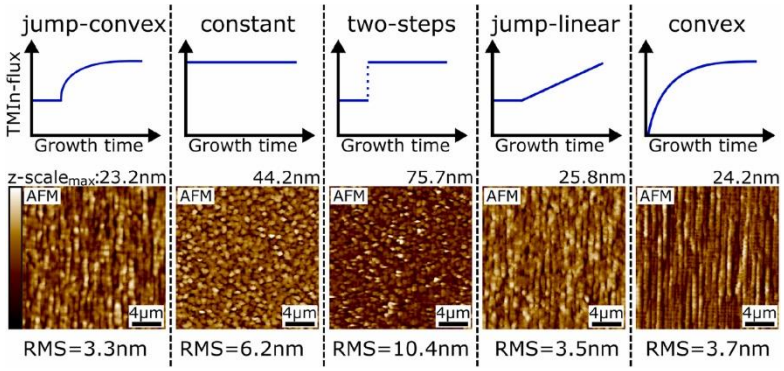

Figure 46: Optimization of growth stage II: Comparison between AFM-scans of various $In_xGa_{1-x}As$ grading profiles to reach 13.2 µmol/min TMIn flux. The constant section used in profiles 1, 3 and 4 has a thickness of 30 nm and the total thickness of each structure is 200 nm. [36]

[43] J. Liu, et al., Nature Nanotechnology 14, 586 (2019).
[44] H. Wang, et al., Physical Review Letters 122, 113602 (2019).
[45] S. Kolatschek, et al., Nano Letters 21 7740 (2021).
[46] S.-W. Xu, et al., Photonics Research 10, 487440 (2022).
[47] A. Barbiero, et al., ACS Photonics 9, 3060 (2022).
[48] L. Bremer, et al., Optics Express 30, 15913 (2022).
[49] A. Barbiero, et al., Optics Express 30, 10919 (2022).
[50] M. Winger, et al., Physical Review Letter 103, 207403 (2009).
[51] J. Liu, et al., Physical. Review Applied 9, 064019 (2018).
[52] G. Shooter, et al., Optics. Express 28, 36838 (2020).
[53] L. Zhai, et al., Nature Communication 11, 4745 (2020).
[54] P. Holewa, et al., ACS Photonics 9, 2273 (2022).
[55] C. Carmesin, et al., Physical Review B 98, 125407 (2018).

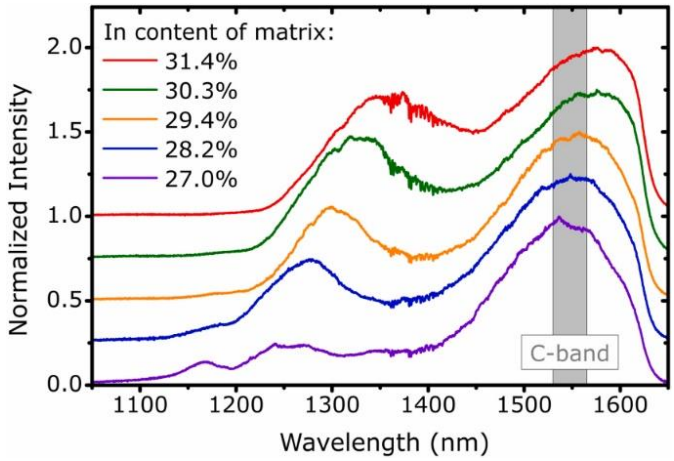

Figure 47: Optimization of growth stage III: Photoluminescence spectra of samples with varying indium content in the $In_xGa_{1-x}As$ matrix around the QDs. The curves are offset vertically for clarity. [36]

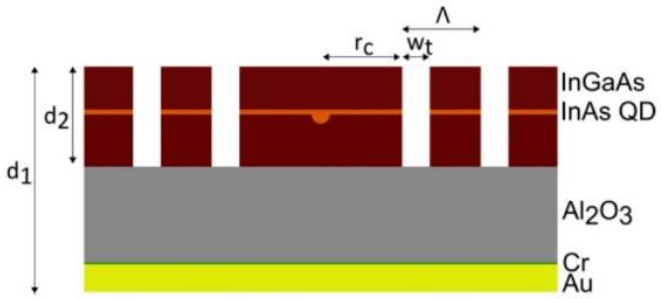

Dimension	Value
r_c	587 nm
w_t	200 nm
Λ	560 nm
d_1	815 nm
d_2	360 nm
Number of trenches	10

Figure 48: Schematic side view of the device structure. For visual clarity only 2 of the 10 trenches are indicated and the horizontal dimension is compressed by a factor of 2 compared to the vertical direction. The table displays the dimensions of the fabricated CBG device [33]

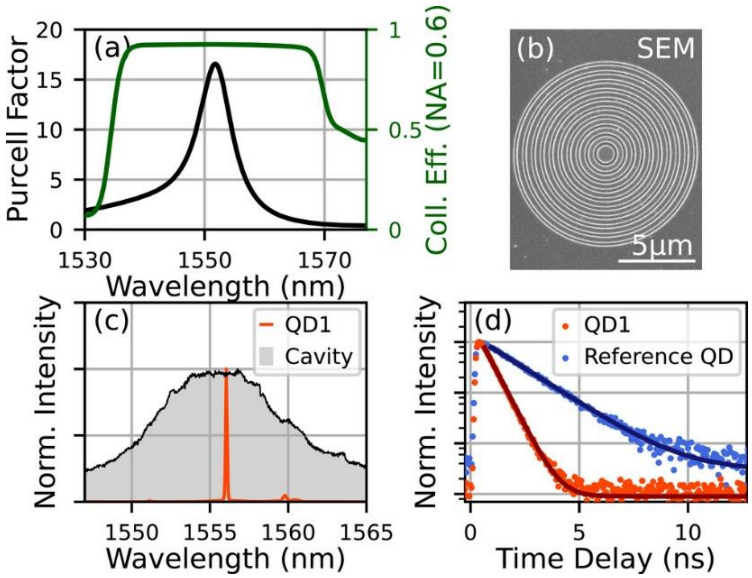

Figure 49: CBG characterisation: a) FDTD simulations for Purcell factor and collection efficiency (NA = 0.6). b) SEM image of the CBG. c) Spectrum of the cavity mode under cw non-resonant pumping (9.5 µW) and of QD1 under p-shell excitation. d) TCSPC measurements with fits (solid lines) under non-resonant excitation at 850 nm of QD1 (decay time 0.52 ns) and a reference QD (decay time 1.59 ns) in a semi-logarithmic scale. [33]

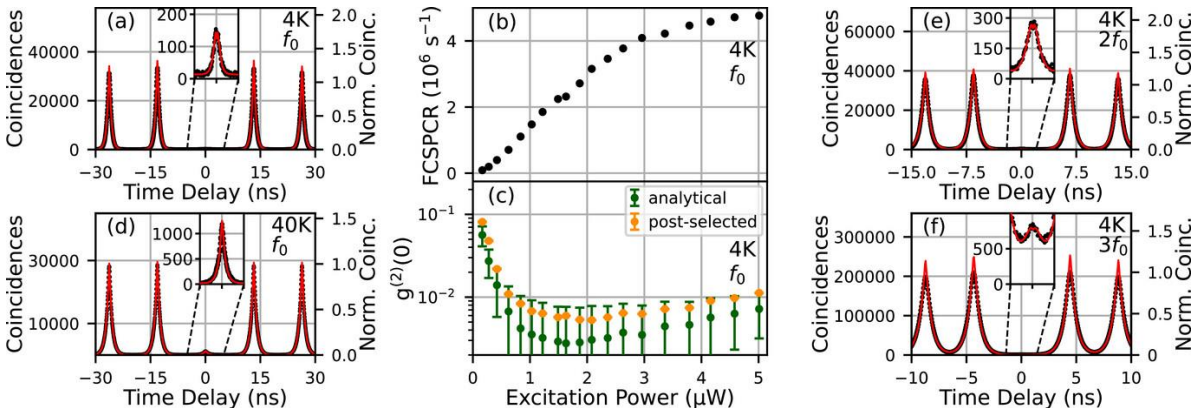

Figure 50: : Brightness and single-photon purity of QD1 under p-shell excitation: a) $g^{(2)}(\tau)$ at 4 K, P = 5.01 μW and f_0 = 76 MHz. b,c) fiber-coupled single-photon count rate (FCSPCR) after the full setup at the detector, corrected for the detection efficiency of 85%, and $g^{(2)}(0)$ over the excitation power. d) $g^{(2)}(\tau)$ at 40 K and P = 5.01 μW. e,f) $g^{(2)}(\tau)$ at 4 K, P = 10.02 μW, $2f_0$ = 152 MHz, and P = 15.03 μW, $3f_0$ = 228 MHz, respectively. [33]

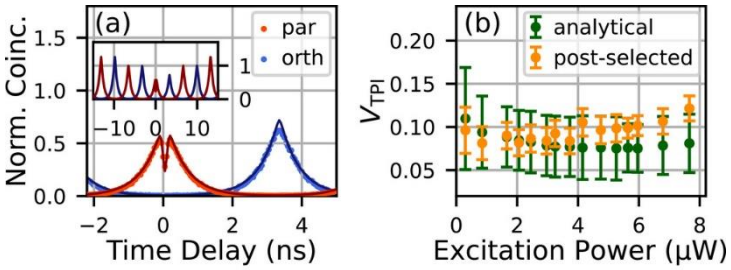

Figure 51: TPI visibility of QD1 under p-shell excitation: a) exemplary TPI measurement for parallel (par) and orthogonal (orth) polarization at P = 7.7 μW. The orthogonal data and fit are offset horizontally for visual clarity. b) V_{TPI} for different excitation powers. [33]

4.3.3.4 Validation of Single-Photon Sources

The validation focused on verifying the spectral characteristics, single-photon purity, photon flux, and other critical parameters of the fabricated sources. For instance, QDs grown on metamorphic buffers and incorporated into planar cavity structures demonstrated photon flux rates up to 11 Mphotons/s and $g^{(2)}(0)$ values below 0.2 under optimal conditions, showing significant promise for practical applications (Figure 52, Figure 53, Figure 54) [56, 57].

Figure 55 shows the photon flux at the position of the detector and the single-photon purity in dependence of the applied excitation power. The linear dependence at low excitation implies that the corresponding spectral line belongs to the recombination of an exciton. Here, the photon flux was calculated by dividing the count rate by the detection efficiency of the SPAD detector used during the measurement. The SPAD detector was calibrated using a reference analog detector and corrected for dark counts and after-pulsing. The measured photon flux was up to (2.55 ± 0.02) × 10^6 photons per second at an excitation power of 3.5 μW. This photon flux corresponds to a radiant flux of (545 ± 4) fW.

[56] R. Sittig et al. Nanophotonics, (2022). https://doi.org/10.1515/nanoph-2021-0552.
[57] S. Rodt and S. Reitzenstein, Nano Ex. 2, 014007 (2021).

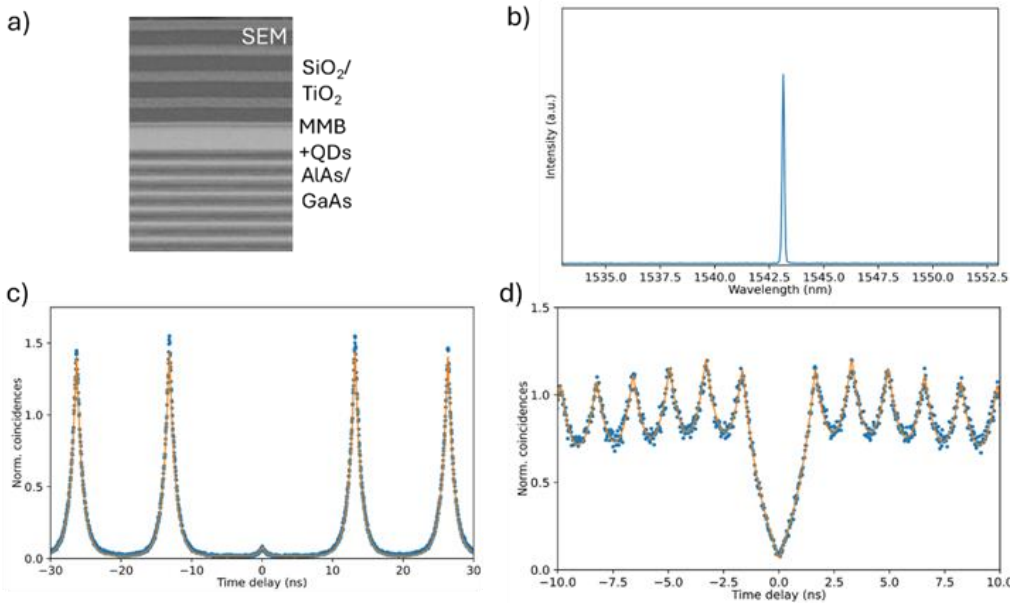

Figure 52: a) SEM side view of the structure of InAs QDs inside an InGaAs-matrix lattice matched to an MMB grown on a GaAs substrate, b) Spectrum of the photon emission after filtering, c) and d) Second-order correlation function determined for pulsed excitation of the QD with a repetition rate of 75.95 MHz and 607.58 MHz, respectively.

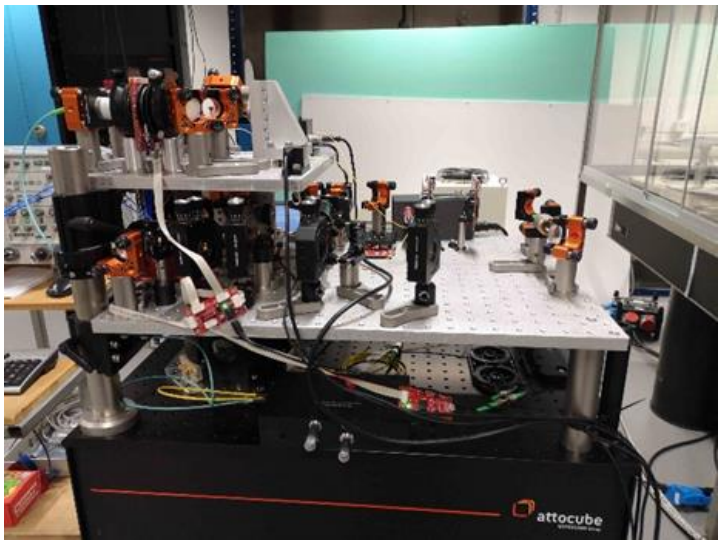

Figure 53: Setup used for the characterization of the QD single-photon emitter developed by USTUTT for C-telecom wavelength (1550 nm).

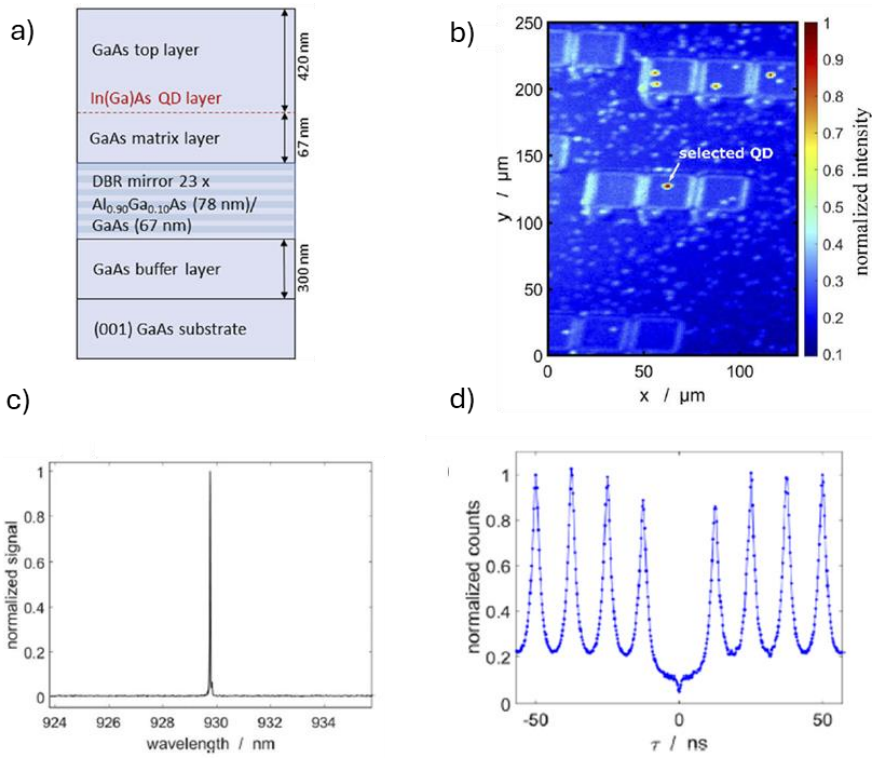

Figure 54: a) Schematic of the sample structure. b) Micro-photoluminescence scan of the sample emission for emission wavelengths above 900 nm. B) c) Spectrally filtered QD µPL emission with a wavelength of λ = (929.8 ± 0.1) nm. d) Second-order correlation measurement for an excitation power of 0.5 µW.

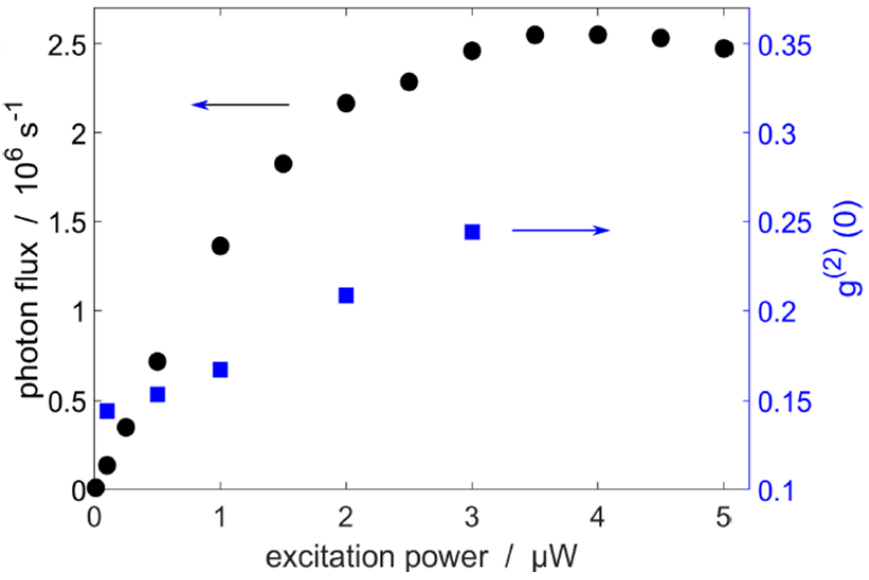

Figure 55: Photon flux (black circles) and single-photon purity (blue squares) of the InGaAs QD based single-photon (@930 nm) source at the position of the SPAD detector.

4.3.3.5 Conclusion

The report documents substantial advancements in the design, fabrication, and optimization of single-photon sources based on semiconductor quantum dots. While significant progress was made towards achieving the target performance specifications, further optimization is needed to meet all objectives fully. The results provide a strong foundation for future developments in quantum technology applications.

4.4 Objective 4

To develop the European metrology infrastructure required for the traceable characterisation of entangled-photon and single-photon sources, i.e. detectors (including photon-number resolving detectors), amplifiers, as well as standardised quantum-optical setups for characterisation (in particular entanglement tomography).

4.4.1 *Executive summary*

The development of a European metrology infrastructure for the traceable characterization of entangled-photon and single-photon sources has achieved significant advancements beyond the current state of the art. This project focused on the traceable characterization of single-photon sources (SPSs) and, particularly, entangled-photon sources, targeting applications in quantum technology, which had not been realized at the National Metrology Institute (NMI) level prior to this initiative.

Key advancements include the development of low-photon flux detectors, photon-number resolving detectors, and associated amplifiers, all of which demonstrate superior performance in terms of detection noise, measurement uncertainty, and stability. Transition edge sensor (TES) detectors, specifically Au/Ti-TES devices, were characterized and achieved high system detection efficiencies of up to 98% and rapid signal decay times below 170 ns at a wavelength of 1548 nm. Additionally, aluminum TES (Al-TES) and gold/titanium TES (Au/Ti-TES) were characterized in cryo-optic facilities, showing significant results in energy resolution, pulse decay time, and system detection efficiency (SDE). Smaller Au/Ti-TES devices (5 µm x 5 µm) showed SDE values around 0.65 to 0.67 with effective time constants between ~220 ns and ~260 ns, while larger devices (12 µm x 12 µm) achieved SDE values up to 0.99 and energy resolutions between 0.46 eV and 0.50 eV.

In the realm of photonic integrated circuits (PICs), new designs were developed that achieved extremely high split ratios (up to 1:10^6) with a relative uncertainty of 1%. These circuits were characterized against a predictable quantum efficient detector (PQED) and a two-channel switched integrator amplifier (SIA), establishing a traceability chain down to a splitting ratio of 1:10^6. Cascading two PICs further extended the capability to achieve split ratios as high as 1:10^10. Moreover, a portable low photon flux calibration facility, capable of handling few femtowatts of power, was created, incorporating these high split ratio PICs.

The project also involved the development of a dual-channel switched integrator amplifier capable of measuring split ratios up to 1:10^6, enhancing the measurement capabilities for photon fluxes and quantum efficiencies. New low-noise, low-photon flux detectors were constructed, calibrated across a spectral range of 580 nm to 970 nm, and demonstrated reliable operation with noise levels at approximately 1%.

Additionally, a confocal measurement system with Time-Correlated-Single-Photon-Counting capability was established for detector calibration using single-photon sources (SPSs). This system, capable of integrating radiation from excited SPSs or externally coupled transportable SPSs, features a Hanbury Brown and Twiss interferometer configuration for photon tracking. Furthermore, a portable semiconductor quantum dot source was developed, housed in a compact 19'' casing with a Stirling cryocooler and a fibre-coupled output. This source achieved fibre-coupling efficiencies up to 24% and count rates exceeding 1 million counts per second, demonstrating its potential for versatile applications in quantum metrology.

These advancements collectively represent a substantial leap forward in metrological infrastructure for quantum technologies, enabling more accurate and reliable characterization of single-photon and entangled-photon sources.

In the following, specific results for the activities focused on in the project with respect to the development of a European metrology infrastructure for the traceable characterisation of entangled-photon and single-photon sources are described in greater detail.

4.4.2 *Integration of TES, characterised for detection efficiency, into a cryo-optic facility optimised for 930 nm and 1550 nm wavelengths*

Within the project, the integration of Transition Edge Sensors (TES) characterized for detection efficiency into a cryo-optic facility optimized for wavelengths of 930 nm and 1550 nm was carried out. The facility, located at PTB's campus in Braunschweig, Germany, was developed with support from multiple institutions including PTB, INRIM, TUB, and AIST/Japan. The integration process involved setting up a SQUID-based readout system and incorporating TES into a cryogenic environment, with contributions from various researchers.

The facility's optical setup consists of fibre-coupled pulsed laser heads that emit light at 930 nm and 1550 nm, configured to produce weak pulses with photon numbers ranging from 0.1 to 10 per pulse. These pulses are attenuated using calibrated fibre attenuators and monitored via a photodiode, enabling accurate calculation of the mean photon number per pulse, see Figure 56.

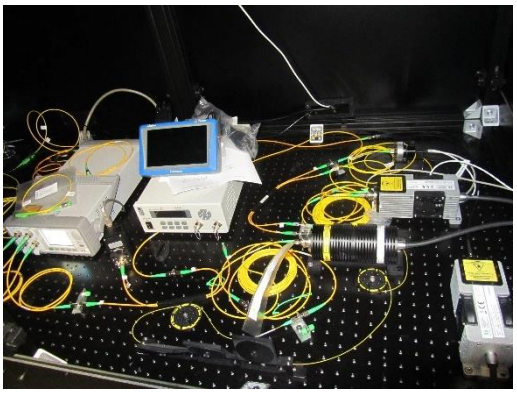

Figure 56: View of the optical setup: on the right-hand side, picosecond laser heads for emissions at different wavelengths such as ~930 mn and ~1550 nm are visible, on the left hand side, the two-stage attenuator can be seen.

The cryogenic component is based on a vacuum dry cryostat, employing a two-stage pulse tube cooler and an adiabatic demagnetization refrigeration (ADR) stage. This configuration allows for achieving temperatures as low as 100 mK, crucial for TES operation. However, due to additional wiring and components, the minimum achievable temperature increased to about 76 mK, and the hold time reduced to seven hours (Figure 57). The setup also includes a custom-built fibre vacuum feedthrough to accommodate multiple fibres (Figure 58). The TES integration involved mounting sensors within the cryogenic environment. The TES modules, including those from AIST (Au/Ti) and INRIM (Ti/Al), were installed on the FAA cooling stage, with each module featuring a fibre-coupled TES chip and a SQUID array for signal readout. The integration process required meticulous heat management to prevent thermal radiation and ensure signal integrity (Figure 59).

Figure 57: View into the cryostat: The large silver 'bin' in the upper part is the Niobium shield around the superconducting ADR magnet; the TES are mounted inside the Titanium box in the lowermost part, which is connected to the FAA cold finger.

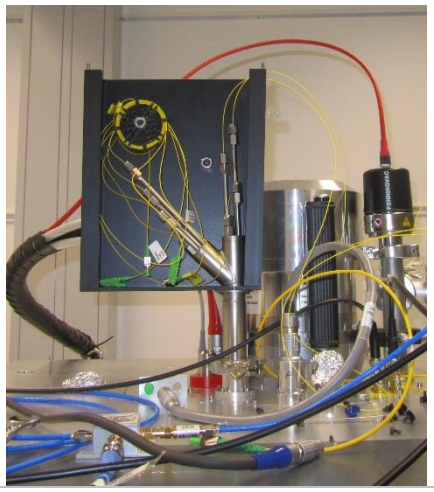

Figure 58: Home-built fibre vacuum feedthrough into the cryostat, accommodating up to eight fibres.

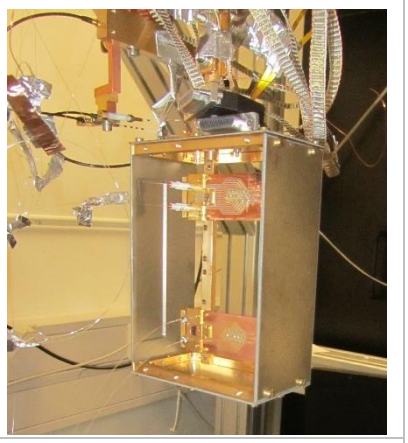

Figure 59: Two TES modules, mounted inside the Titanium box at the FAA stage; upper part: TES module containing two sensors manufactured by AIST/Japan (Au/Ti); lower part: TES module containing two sensors manufactured by INRIM/Italy (Ti/Al).

Within the project, several challenges were identified, primarily related to cryogenic wiring and the reliability of the thermal switch, which requires frequent realignment due to sensitivity to magnetic fields. Additionally, direct

fibre coupling to TES chips proved to be fragile, necessitating careful handling and heat sinking to maintain system performance. The characterization of TES at 1550 nm was performed using the facility. The analysis included energy resolution, pulse decay time, and system detection efficiency. For instance, the TES from AIST showed varied detection efficiencies and response times under different conditions, demonstrating the setup's capability for detailed TES performance evaluation (Figure 60 and Figure 61).

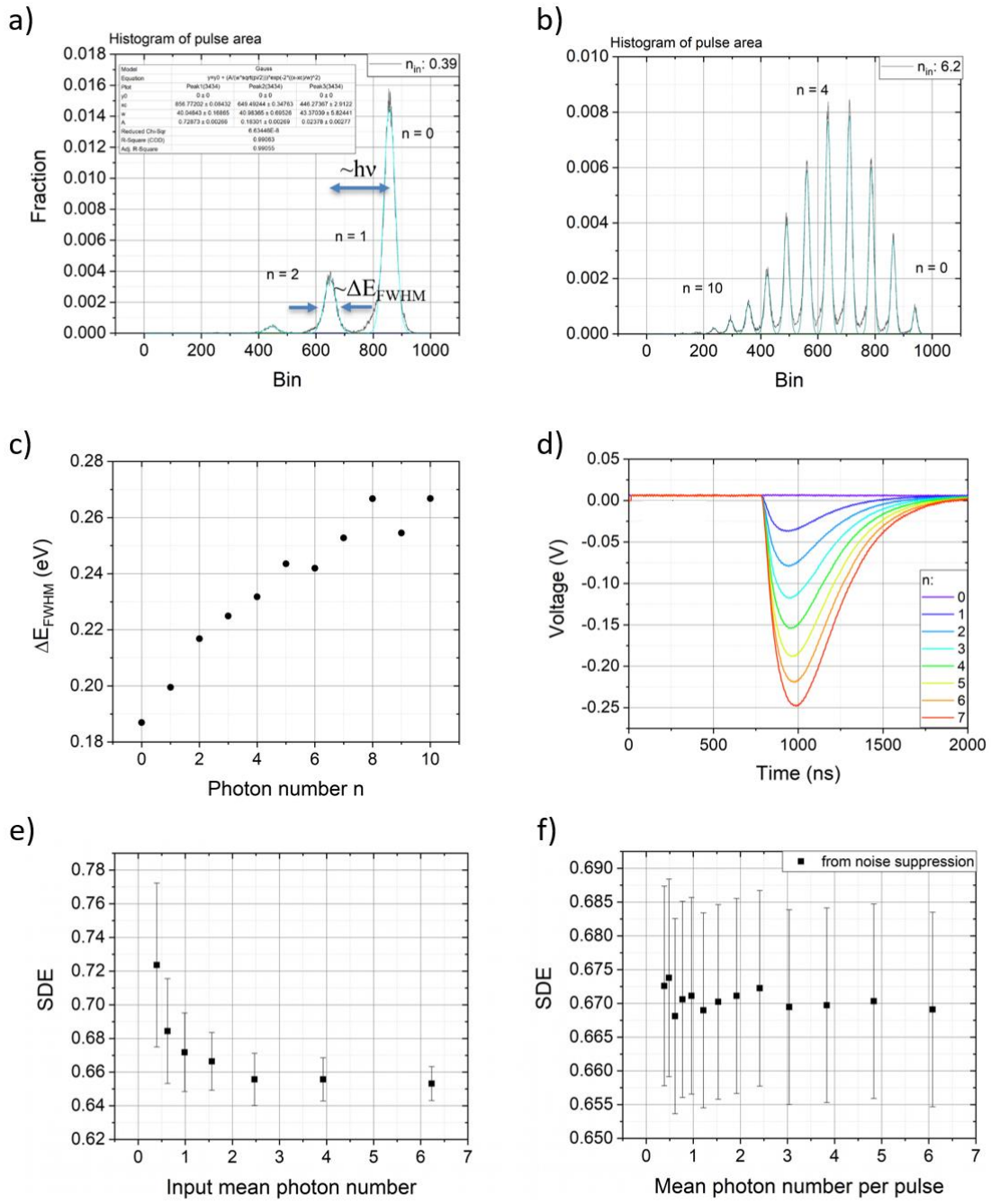

Figure 60: Characterisation of TES ST164-b3 (Au/Ti, 5 µm x 5 µm, provided by AIST): a), b) probability distribution of the detection pulse areas for two different incoming mean photon numbers; c) full width at half maximum of the respective peaks in the distribution in (eV); d) (averaged) pulse shapes for the individual number states (T: 105 mK), where a fit to the effective time constants between ~220 ns and ~260 ns; e), f) system detection efficiency of the fibre coupled TES at 1550 nm (1548 nm), as determined from the amplitudes in the histogram (e) and the time tagger based analysis of the suppression of non-signal counts (f).

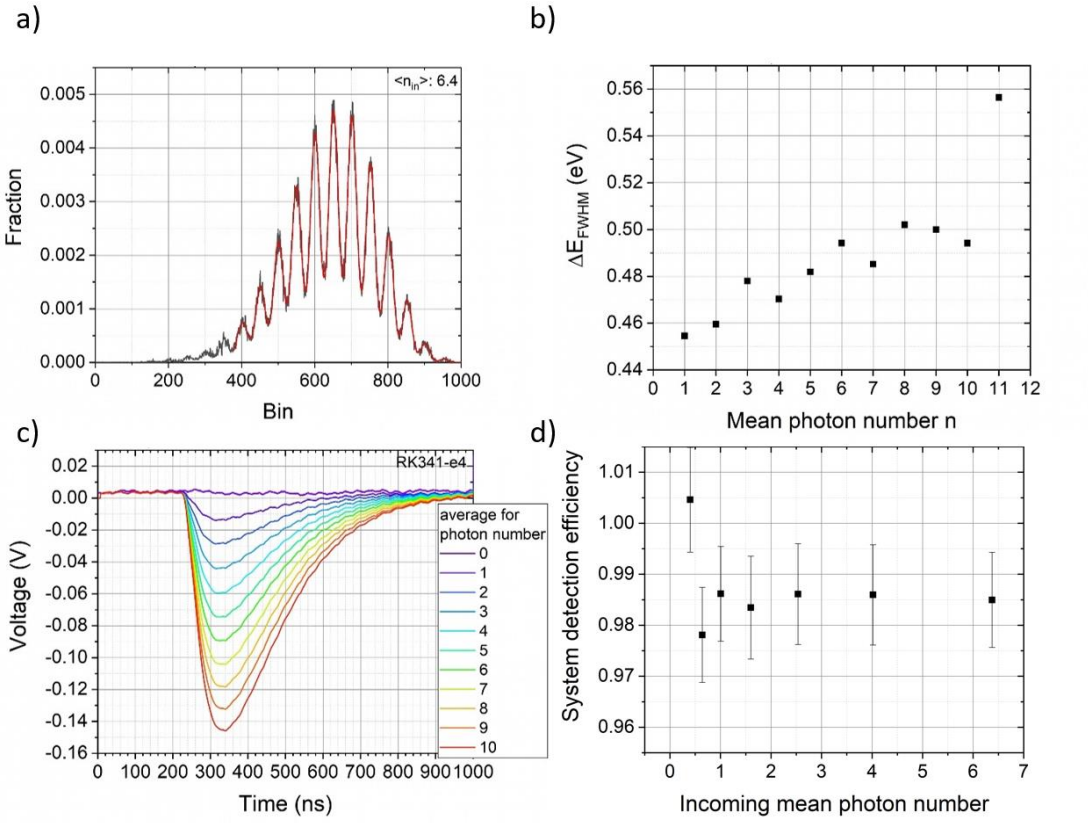

Figure 61: Characterisation of TES RK341-e4 (Au/Ti, 12 µm x 12 µm, provided by AIST): a) probability distribution of the electric detection pulse areas for two different incoming mean photon numbers; b) full width at half maximum of the respective peaks in the distribution in (eV); c) (averaged) pulse shapes for the individual number states (T: 90 mK), where a fit to the decaying flank yields time constants between ~160 ns and ~175 ns; d) system detection efficiency of the fibre coupled TES at 1550 nm (1548 nm), as determined from the amplitudes in the histogram.

INRiM focused on enhancing aluminium TES, aiming to reduce effective time constants and improve transition temperatures. Several batches were produced to optimize these properties, with notable success in minimizing issues like aluminium oxide formation, which hindered device performance. The optimized TES achieved response times below 50 ns, a significant improvement for metrological applications (Figure 62).

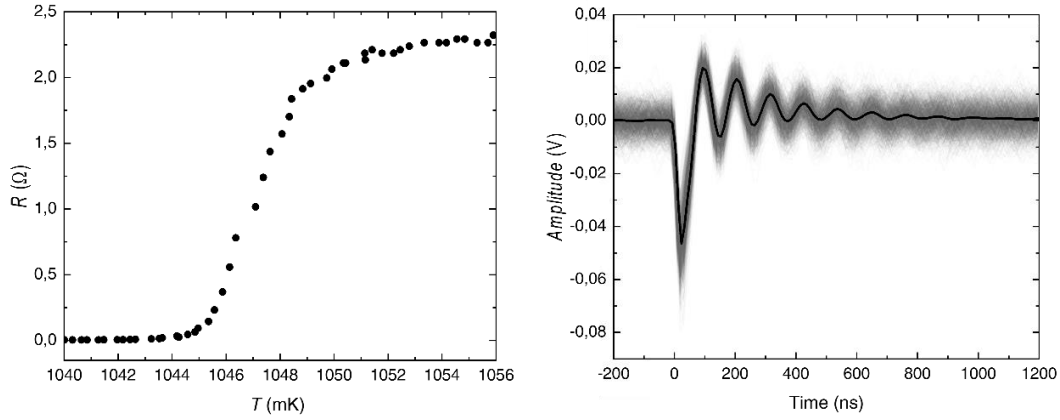

Figure 62: Superconducting transition of a 7×7 µm² Al Transition Edge Sensor (TES) is illustrated on the left. The right side displays the superposition of 10,000 pulses in gray, with the average pulse shown in black. These outcomes were achieved by illuminating the TES with a pulsed monochromatic laser at a constant power emitting at 1540 nm. The TES was polarized at 60% of its normal resistance.

For the outlook, the cryo-optic facility is set for further enhancements, including expanding its wavelength capabilities and improving the thermal switch's reliability. Plans are also underway to segregate cryogenic setups to reduce wiring complexity and thermal mass, thereby enhancing the facility's versatility for future TES characterization and quantum metrology research.

4.4.3 *Novel Measurement Techniques and Applications for Metrological Characterization of Photon Sources*

Within the project the development and application of novel measurement techniques and infrastructure for the metrological characterization of single-photon and low photon flux sources at various European National Metrology Institutes (NMIs) was addressed. This effort is part of a broader initiative to build a European metrology infrastructure capable of traceable characterization of photon sources, including photon-number resolving detectors, amplifiers, and standardized quantum-optical setups. The main objectives included the development of cryo-optic measurement facilities for photon number resolving detectors, novel detector calibration techniques, and calibration setups for single-photon detectors and sources. These aims were largely achieved, with several NMIs now equipped with advanced setups for traceable characterization of single-photon and entangled-photon sources.

4.4.3.1 Novel Techniques for Detector Calibration: Development and Characterization of PIC-Splitter

The project developed a photonic integrated circuit (PIC) splitter capable of achieving a high splitting ratio of up to 1:10^6 with a relative uncertainty of 0.5% across a wavelength range of 600-950 nm (Figure 63). The PIC splitter, consisting of six cascaded multimode interference (MMI) couplers, allows precise division of incoming light for low power calibration. This setup is crucial for extending traceability to very low optical powers, supporting the calibration of photon detectors in the low photon flux regime.

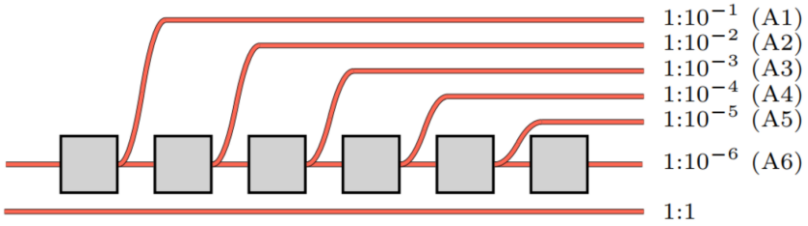

Figure 63: Schematic layout of the cascaded MMI splitter chip. The grey boxes represent the MMI couplers and the orange lines represent the optical waveguides.

The characterization of the splitter involved testing the stability of the splitting ratio under varying polarization conditions. Results indicated significant variability depending on polarization, with the difference between maximum and minimum ratios ranging from 16 % to 240 % (Figure 64a). Adjusting polarization to optimize output stability improved measurement consistency (Figure 64b).

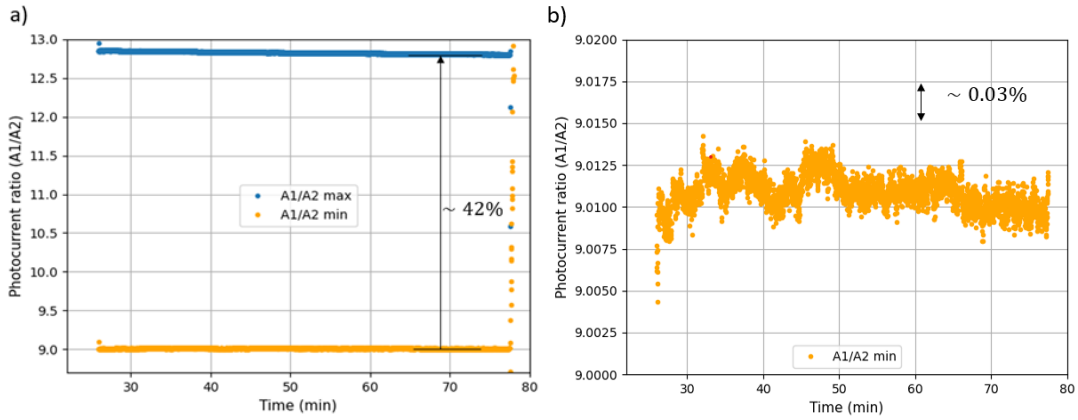

Figure 64: Time series of the A1 and A2 channel pair ratio measured using the Thorlabs photodiodes. a) The maximum and minimum ratio from changing the polarization. b) The stability of the ratio after the polarization has been optimized to minimize the ratio A1/A2.

An experimental setup using the PIC splitter was constructed to measure low-power optical signals. The setup included a fibre-coupled Thorlabs FPV852P laser, attenuators, and polarization controllers to ensure stable

and replicable measurements (Figure 65). A comparison campaign between JV and CMI was conducted to validate the developed measurement capabilities, using JV's PQED and PIC splitter and CMI's two-channel switched integrator amplifier (SIA) detector. Discrepancies in the measured ratios between JV and CMI were observed, possibly due to transportation-induced changes, underscoring the need for robust handling protocols (Figure 66).

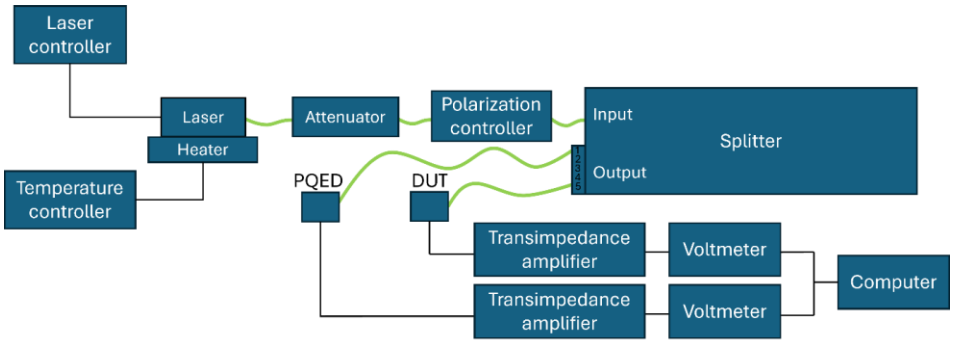

Figure 65: Experimental setup. The green lines represent optical connections and the black lines represent electrical connections.

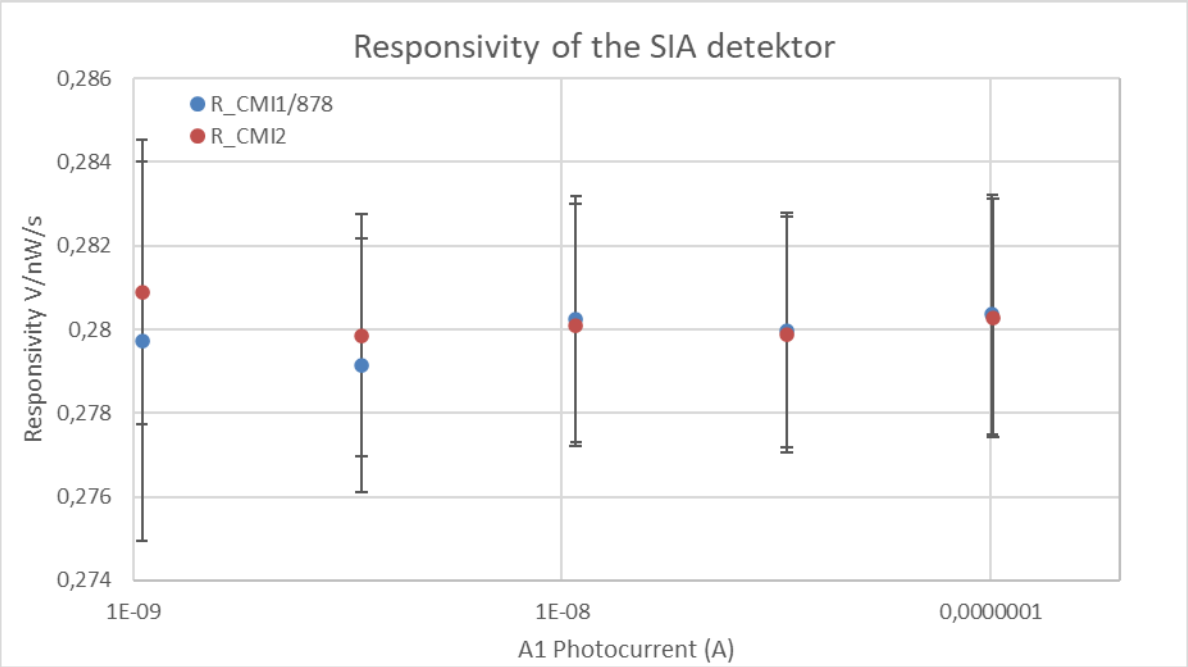

Figure 66: Responsivity of the SIA detector as a function of the photocurrent on the A1 channel. The blue values are for the amplified channel and the orange values are for the base channel.

4.4.3.2 Single-Photon Detectors and Sources for Calibration Purposes:

4.4.3.2.1 Low Photon Flux Detectors and their Calibration

Low photon flux photodetectors, such as the KBFI detector, were developed to measure weak optical signals with high accuracy and linearity across several orders of magnitude (Figure 67, Figure 68, Figure 69). The KBFI detector, a silicon photodiode-based device cooled with liquid nitrogen, was tested against single-photon sources and attenuated lasers. Comparative studies with reference detectors showed that the KBFI detector maintained good agreement with established standards (Table 4, Table 5).

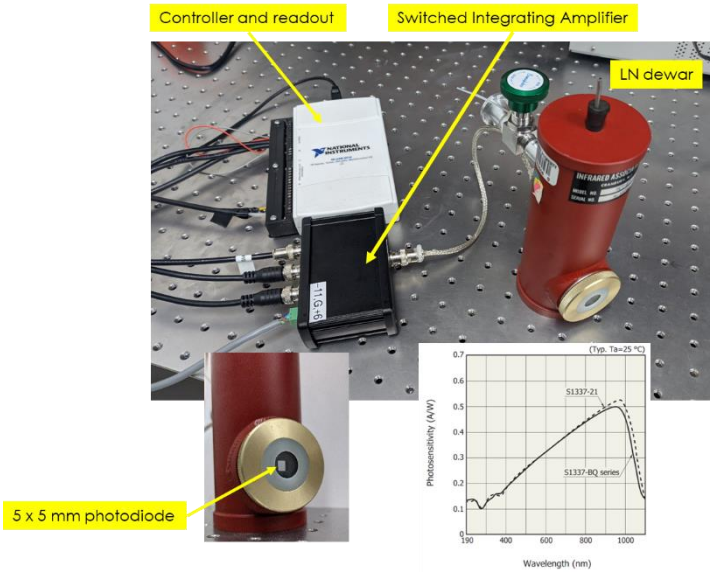

Figure 67: KBFI detector for low photon flux measurements

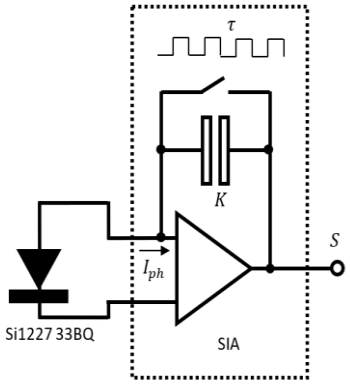

Figure 68: CMI reference detector scheme

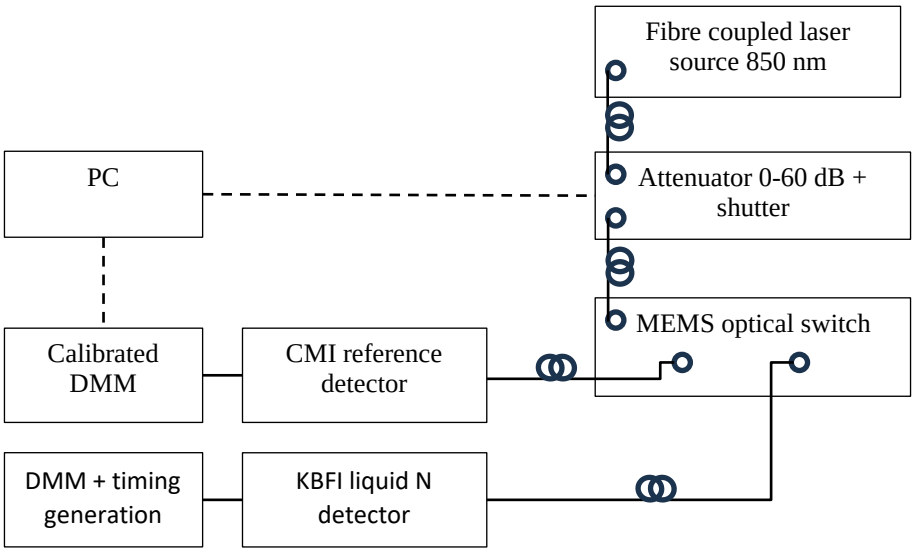

Figure 69: Experimental setup scheme for KBFI detector and CMI reference detector comparison.

Table 4: Comparison of the KBFI detector with TU-Berlin fibre-coupled SPS2. Comparison was done by switching fibre in front of a SPAD detector and in front of KBFI detector

SPS 2				
Source: InGaAs Quantum Dot at 923.8 nm, in helium can; excitation laser Ti:Sapphire at 851nm				
KBFI detector, Estimated photon flux (million/s)	Standard uncertainty of measurements with KBFI detector	TUB SPS, estimated photon flux (million/s)	Standard uncertainty of TUB detector	photon count ratio KBFI vs TUB SPS
0.045	9%	0.058	1.1%	0.77

Table 5: Measurements of the KBFI detector using attenuated laser at TU Berlin

Attenuated laser				
Source: TUB Ti:Sapphire attenuated laser at 904 nm (80Mhz)				
KBFI detector, estimated photon flux (million/s)	Standard uncertainty of measurements with KBFI detector	TUB source, estimated photon flux (million/s)	Standard uncertainty of TUB detector	photon count ratio KBFI vs TUB
2.927	2.2%	2.849	1.8%	1.03
1.223	3.1%	1.225	1.8%	1.00
1.218	3.3%	1.254	1.8%	0.97
0.394	7.5%	0.413	1.8%	0.95
0.398	6.0%	0.413	1.8%	0.96
0.421	13.0%	0.413	1.8%	1.02

Calibration was extended using Predictable Quantum Efficiency Detectors (PQED), achieving linearity over a broad range of photon flux levels (0.5 million to 10 million photons per second), with uncertainties below 1% (Table 6, Figure 70). These findings confirm the detectors' suitability for precise metrological applications, ensuring reliable photon counting and flux measurements.

Table 6: Results of PQED and KBFI detectors measuring several photon flux levels between 0.5 Mph/s and 10 Mph/s. The measured photon rate of KBFI detector is based on nominal responsivity of the photodiode.

Measured photon rate with PQED, million ph/s	Standard uncertainty of PQED	Measured photon rate of KBFI detector, million ph/s	Standard uncertainty of KBFI detector	Correction factor KBFI detector / PQED
0.50	3.71%	0.49	2.50%	**0.984**
1.20	1.83%	1.18	1.85%	**0.983**
2.41	1.18%	2.40	0.80%	**0.997**
5.03	0.83%	5.02	0.76%	**0.999**
10.13	0.70%	10.04	0.75%	**0.991**

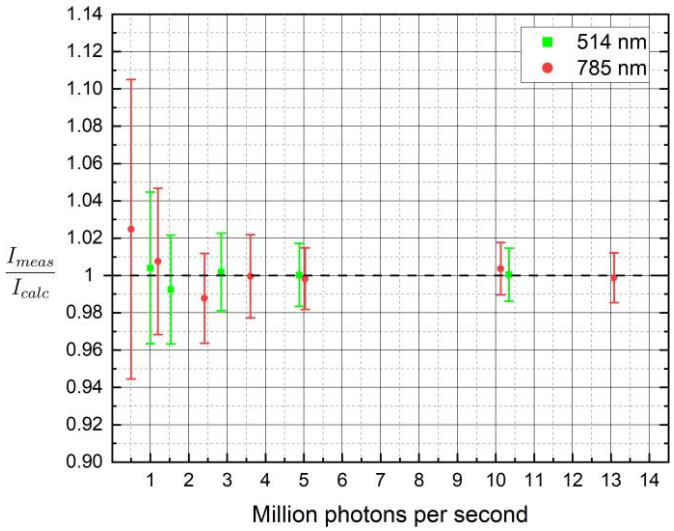

Figure 70: Ratio of measured and expected photocurrent at different photon flux levels corresponding to optical power range from 130 fW to 3.3 pW. The error bars are given at 95% confidence level.

4.4.3.2.2 Improved Measurement System for SPS and Detector Studies

Within the project, the development of a sophisticated measurement setup incorporating a time-resolved confocal fluorescence microscope with Time-Correlated-Single-Photon-Counting capability (Figure 71) was addressed. This system supports the detailed study of low-photon flux detectors and single-photon sources (SPS), providing both free-space and fibre-coupled measurement options.

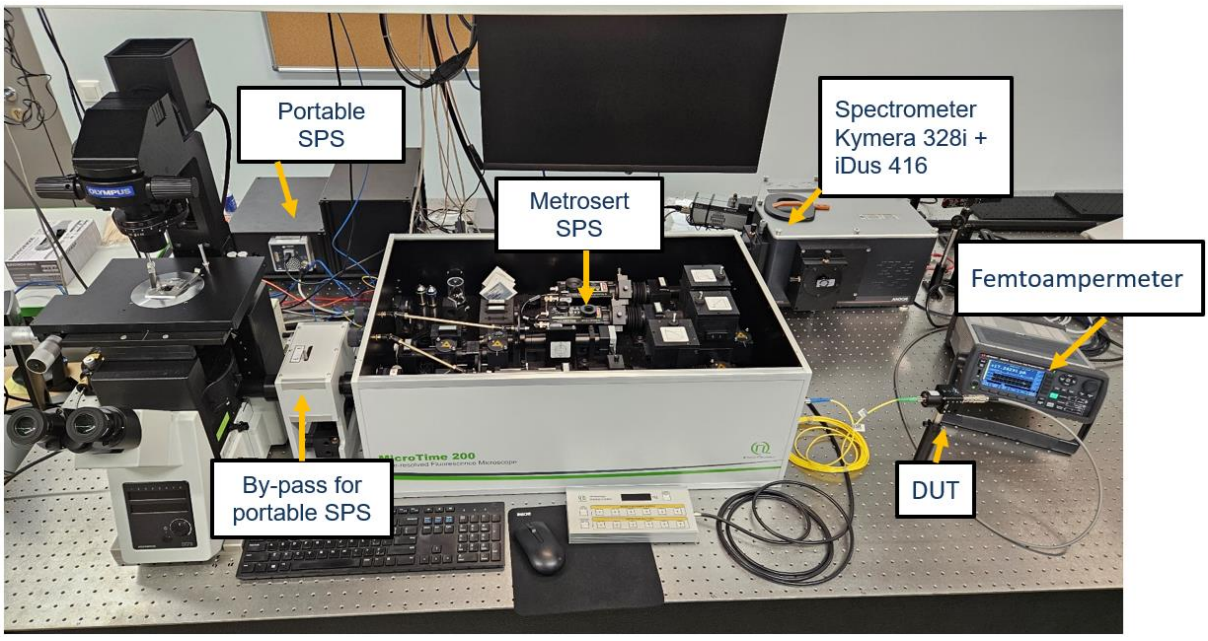

Figure 71: The measurement set-up with Time-Correlated-Single-Photon-Counting capability for using portable or in-house realised single-photon-source (SPS) in characterization of low-photon flux detectors developed at Metrosert. Alternatively, SPS can be metrologically studied by using the spectrometer and a reference detector.

4.4.3.2.3 Pulsed Mode Linearity Measurements

Two methods were developed to evaluate the linearity of detectors in pulsed mode: a beam-addition technique and a method assessing linearity across varied pulse rates (0.03 - 10 MHz). The beam-addition method, using fibre-optic components at a fixed pulse rate of 10 MHz, demonstrated nonlinearity within ±0.02 over two orders

of magnitude in photon flux, with uncertainties ranging from 0.08 to 0.009 (Table 7, Figure 72). The varied pulse rate method showed that the KBFI detector maintained high linearity (R^2 = 0.999973) across different repetition rates, affirming its capability for accurate photon detection in dynamic conditions (Table 8, Figure 73).

Table 7: Repeated nonlinearity tests of the KBFI detector in the photon flux range from 0.5 Mph/s to 50 Mph/s with the measurement set-up developed at Metrosert by using picosecond pulsed laser model LDH-D-C-690 at the wavelength of 685 nm at the repetition frequency 10 MHz.

	1st round				2nd round			
	$i_{CH1,k}$	$i_{CH2,k}$	$i_{(CH1+CH2),k}$	NL	$i_{CH1,k}$	$i_{CH2,k}$	$i_{(CH1+CH2),k}$	NL
	fA	fA	fA		fA	fA	fA	
1	-67.8	-76.5	-143.3	-0.007	-28.4	-32.9	-60.2	-0.020
2	-99.7	-114.2	-212.4	-0.007	-66.7	-59.1	-125.1	-0.006
3	-163.5	-187.3	-350.3	-0.001	-133.3	-118.3	-250.7	-0.004
4	-289.9	-330.9	-620.9	0.000	-275.2	-244.5	-518.6	-0.002
5	-521.3	-595.4	-1115.3	-0.001	-537.3	-477.0	-1013.6	-0.001
6	-1074.2	-1226.8	-2298.8	-0.001	-1072.1	-951.4	-2023.6	0.000
7	-3895.8	-4451.2	-8371.7	0.003	-2133.8	-1894.2	-4033.0	0.001
8					-4320.2	-3831.6	-8196.3	0.005
9					-8577.0	-7607.1	-16240.0	0.003

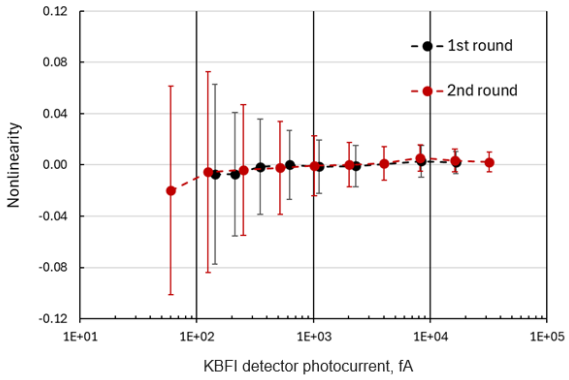

Figure 72: Repeated nonlinearity tests of the KBFI detector in the photon flux range from 0.5 Mph/s to 50 Mph/s with the measurement set-up developed at Metrosert. Vertical bars indicate combined standard uncertainty of measurement results.

4.4.3.3 Conclusion

The project successfully advanced the metrological infrastructure for quantum technologies, developing novel measurement techniques and facilities for the traceable characterization of photon sources. The achievements include the enhancement of TES detector capabilities, the development of a high-precision PIC splitter for low photon flux calibration, and the creation of advanced setups for single-photon detection and source calibration. These innovations will significantly improve the accuracy and reliability of photon measurements across European NMIs, supporting further advancements in quantum metrology and fundamental physics research.

Table 8: Measured photocurrents of KBFI detector at different laser repetitions rates. The accompanying figure shows the same data on a graph indicating also the linear fit coefficient R^2

Pulse rate, MHz	Measured photocurrent, fA
0.03125	124.05
0.0625	250.32
0.125	500.45
0.25	1005.26
0.5	2013.85
1	4026.99
2.5	10177.91
5	20650.35
10	40899.14

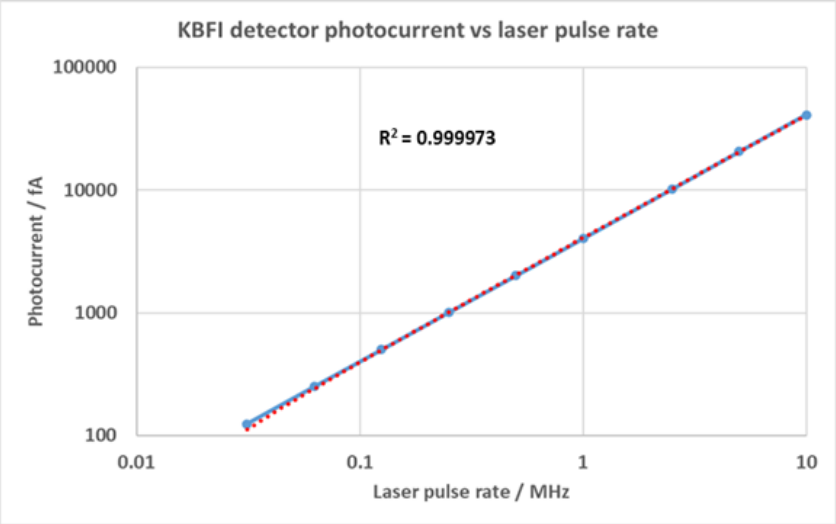

Figure 73: KBFI detector photocurrent vs. laser pulse rate.

5 Impact

(Please leave this section blank. This section will be completed by the EURAMET MSU using text from the final Publishable Summary.)

6 List of publications

(Please leave this section blank. This section will be completed by the EURAMET MSU using text from the final Publishable Summary.)

7 Contact details

Coordinator:

Stefan Kück, PTB

Tel: +49 531 5924010

E-mail: stefan.kueck@ptb.de

Project website address: https://www.sequme.eu/

Please delete before you submit your report

Document Control Page

Document Title:	EMPIR Contracts Reporting Template 6: Final Publishable Report	
Document Code:	P-CON-TMP-106	Version 1.5
Document Control:	Approved: Programme Manager	2021-07-23